Investigation of Resonators Loaded Periodic Structures

by

M'baye Diao

B.S., Electrical Engineering
Syracuse University, 2004

Submitted to the
Department of Electrical Engineering and Computer Science
in partial fulfillment of the requirements for the degree of

Master of Science

at the

MASSACHUSETTS INSTITUTE OF TECHNOLOGY

February 2006

Author..... .....
Department of Electrical Engineering and Computer Science
January 25, 2006

Certified by..... .....
Jin A. Kong
Professor of Electrical Engineering
Thesis Supervisor

Certified by.. .....
Bae-Ian Wu
Research Scientist
Thesis Supervisor

Accepted by..... .....
Arthur C. Smith
Chairman, Department Committee on Graduate Students

Investigation of Resonators Loaded Periodic Structures

By

M'baye Diao

Submitted to the Department of Electrical Engineering and Computer Science
on January 25, 2006, in partial fulfillment of the
requirements for the degree of
Master of Science in Electrical Engineering and Computer Science

Abstract

The study of metamaterials has brought about new changes in modern microwave communication systems. As predicted by Veselago some 37 years ago, substances which exhibit simultaneously, negative permittivity (ε) and negative permeability (μ) over a certain range of frequencies would display some unusual phenomena such as backward waves, reversed refraction, backward Cerenkov radiation, and negative refractive index. Because of these new features of left handed materials, many structures such as split rings resonators (SRR) have been proposed in the literature to artificially fabricate radio frequency and microwave components. Due to their bulk properties, periodic arrays of SRRs provide a negative permeability. Therefore under the fundamental limit of effective medium theory that the dimensions of the lattice are much smaller than the wavelength, we can treat the array of SRRs as bulk material and retrieve its effective parameters. Also because of size reduction and selective passband transmission spectra in planar geometry, split rings resonators are designed under the fundamental limit (dimensions of one-tenth of the wavelength or smaller), and as a result they constitute better candidates than their L-C loaded transmission lines counterparts for microwaves applications. The generalized formula for impedance-loaded transmission line is derived. The dispersion characteristic and impedance of structures with periodic resonators are analyzed as well.

Thesis Supervisor: Jin A. Kong
Title: Professor of Electrical Engineering

Thesis Supervisor: Bae-Ian Wu
Title: Research Scientist

Acknowledgments

My first and last thanks go out to Allah the Almighty Who has given me the strength and determination to carry out this thesis work. I thank my advisor Professor Jin A. Kong for being very supportive throughout the entire process. I equally thank Dr. Bae-Ian Wu, for not only co-supervising my thesis, but also for spending a good amount of time in editing and making sure that the results are accurate. I cannot really find words to thank him. He has been very helpful throughout the entire thesis process. I am very grateful to him.

I also thank my parents, my wife and children who were all very patient with me during all this period of hardship that I had to stay away from them. I thank them for their prayers and their moral support and good will.

Contents

List of Figures

Chapter 1

Introduction

1.1 Problem Statement

Since Veselago [1] predicted that a medium in which both the permittivity (ε) and permeability (μ) are simultaneously negative, the study of Left-handed material has been the subject of controversy. There have been hot debates over the topic whether or not such medium could, in fact host propagation of electromagnetic waves. Until 1999, there was not too much curiosity about the topic, due to the simple fact there was not any experimental verification to Veselago's postulation. However since 1999, John Pendry [2] et al have proposed the split-ring resonator, which, if driven to its resonant frequency could display a frequency band in which the real part of (μ) is negative. It is known that the wire medium exhibits a frequency band in which the real part of the permittivity is negative, therefore if one could lower the magnetic resonant frequency of the split-ring in such a way that it will overlap with the negative epsilon of the infinite metallic wires, one would be able to fabricate a composite material or metamaterial. This was Pendry's main idea about and has become the prototype in obtaining (μ) negative.

Because we have not yet encountered any such material in nature, the above suggestion seems to be working very well for many people. As a result Smith et al [3-6] have taken the task to experimentally fabricate a metamaterial and verified its unique properties among others, reversal of Snell's law, backward wave, reversed Doppler shift, negative index of refraction. In addition to this, by using a slab of metamaterial, one will be able to focus perfectly the image of an object. Moreover, we will be able to have sub wavelength

focusing, but also there will be new possibility of fabricating perfect lenses [7-9]. All of these are due to the property of metamaterials.

Although the split ring resonator and the rod was one of the first designs in the realization of metamaterial, some of today's fabrication is solely based on split rings only without the rod. The reason being that a better understanding of the structure has been developed, that in addition to their magnetic resonant frequency, SRR also have electric resonant frequency due to the mutual coupling between the loops [10-12]. Therefore the progress in left handed material has gone from rings and rods to two splits rings resonators (SRRs) diametrically opposite in order to achieve strong coupling between the rings, since we are trying to lower the magnetic resonant frequency. And this is one way of doing it by increasing the inductance or the capacitance of the structure.

Due to the bianisotropic effect of the edge side coupled, improved performance had been proposed by Marqués et al [11-12] that led to the design of the broadside coupled structure. Contrary to the common view that left-handedness was mainly characterized by the peak of the transmission spectra being within the stop bands of the SRRs alone and wires alone, Kafesaki et al [13-15] have demonstrated that this was not always the case. Rather for the composite metamaterial, the criterion for left-handedness is such that the peak of the transmission spectra should be located above the magnetic resonant frequency, caused by the split in the ring and the loop, and below the electric plasma frequency of the single SRR, since the electric response of the SRR is equivalent to that of cut wires. In addition to the orientation of the SRR with respect to the incident electromagnetic wave, one can achieve electric, magnetic, or both electric and magnetic coupling. These different couplings introduce bianisotropic effects that are undesirable in the structure, and improved retrieval results have been obtained [16]. Since the close ring also presents a dip in its transmission spectra, therefore to lift the ambiguity, Soukoulis et al have conducted different experiments with two different rings with the same size and same geometry. The only difference was that one ring is split whereas the other is closed. The results show that both rings present the same dip in the same frequency band identified as a plasma frequency corresponding to ε negative in the higher frequency band

whereas there was a dip observed only in the transmission spectra of the SRR in the low frequency range, corresponding to μ negative. This led Soukoulis et al to conclude that the split in the ring is essential to the left-handedness, since the closing of the split will destroy the first dip in the transmission spectra corresponding to μ negative.

It can be seen from these different arguments, that in order to have a LH band, one must be able to control both the magnetic and electric resonant frequencies of the SRR. In addition, one should be able to tune the electric resonant frequency to fall between the magnetic resonant frequency of the SRR and its plasma frequency. The first step in doing so would be to understand and study the dependence of the electric resonant frequency ω_0, and the magnetic resonant frequency ω_m as a function of the geometry parameters. Since simulation results have shown a strong dependence of the resonance frequency of SRR as functions of gap width, metal thickness, orientation and size [17].

To better understand the concept of LHM, let us resort to Maxwell equations. Assuming continuous waves, we know that the electromagnetic waves are time harmonic and therefore the time dependence can be eliminated. Assuming all fields quantities to be of the form $e^{i(\vec{k}\bullet\vec{r}-\omega t)}$, we can write Maxwell equations as [19]:

$$\vec{k}\times\vec{E}=\omega\mu\vec{H} \quad (1.1)$$
$$\vec{k}\times\vec{H}=-\omega\varepsilon\vec{E} \quad (1.2)$$
$$\vec{k}\bullet\vec{E}=0 \quad (1.3)$$
$$\vec{k}\bullet\vec{H}=0 \quad (1.4)$$

It is seen from equations (1.1) and (1.2) that whenever μ and ε are both positive the triplet $\left(\vec{E},\vec{H},\vec{k}\right)$ form a right-handed triplet, and whenever both μ and ε are negative, then the triplet $\left(\vec{E},\vec{H},\vec{k}\right)$ form a left-handed triplet. The vector Poynting's power density can be written as follows:

$$\vec{S}(\vec{r},t) = \vec{E} \times \vec{H} = \frac{1}{\omega\mu} \vec{E} \times (\vec{k} \times \vec{E}) \cos^2(\vec{k} \bullet \vec{r} - \omega t)$$

$$\Rightarrow \vec{S}(\vec{r},t) = \frac{1}{\omega\mu} \vec{k} \left|\vec{E}\right|^2 \cos^2(\vec{k} \bullet \vec{r} - \omega t) \qquad (1.5)$$

And the time-average vector power density is:

$$\left\langle \vec{S}(\vec{r},t) \right\rangle = \frac{1}{2\pi} \int_0^{2\pi} d(\omega t) \frac{1}{\omega\mu} \vec{k} \left|\vec{E}\right|^2 \cos^2(\vec{k} \bullet \vec{r} - \omega t) \Rightarrow \left\langle \vec{S}(\vec{r},t \right\rangle = \frac{1}{2\omega\mu} \vec{k} \left|\vec{E}\right|^2 \quad (1.6)$$

From equation (1.6), it is obvious that if both ε and μ are positive, then the time-average Poynting's power density is in the same direction as the wave vector $\vec{k}$, and opposite to each other in the case where both ε and μ are simultaneously negative. As a result, the index of refraction $n = \sqrt{\mu(\omega)\varepsilon(\omega)}$ is negative in certain frequency band. Therefore, phase and group velocity of an electromagnetic wave propagate in opposite direction to that of energy flow. This phenomenon also known as negative refraction has been theoretically proposed by Veselago back in 1968 [1]. Unfortunately, there was not much experimental verification done at that time to support his postulation. It was until late in 2000 that Smith et al [3, 4, 5, 6] reported the experimental demonstration of LHM by stacking arrays of thin wires structures and SRRs in 1D and 2D structures to form a composite metamaterials (CMM).

Although negative refraction and left-handed behavior can be achieved by using 2D photonic crystal, the present study will mainly focus on characterizing and identifying left handed behaviors (both ε and μ are simultaneously negative) in the study of resonators loaded periodic structures. One way of achieving negative effective permittivity is to use periodic thin wires media. The challenge was then getting a negative effective permeability. Fortunately in 1999, John Pendry [2] proposed the array of split ring resonators, which exhibit negative effective μ for frequencies near and above the magnetic resonant frequency of the SRR.

1.2 Thesis Outline

In Chapter 2, we talk about transmission lines modeling of resonators loaded periodic structures, we provide a parallel study between the real transmission lines and the lumped elements transmission lines, as well as a thorough analysis of the periodically loaded transmission lines using the transfer matrices method. We derive the dispersion relation using the ABCD matrix, and from it we derive the normalized Bloch impedance of the unit cell. In section 2.3, we provide a generic formula for any loading configuration by deriving the effective parameters of a T network. Section 2.4 deals with different cases studies for different loading such as, capacitive loading, inductive loading, and any possible combination of the two.

Chapter 3 deals with the actual design of our proposed structure. We first provided a flow chart about how we are going to proceed for the analysis of the structure. Afterwards, we tested our method by applying our analysis to a published structure by retrieving its effective parameters in both subsections 3.1.2 and 3.1.3. In section 3.2, we recalled some of our research in split-rings resonators, namely the S-structure, and the symmetric rings.

Chapter 4 deals with the design of the single ring structure that display negative permeability behavior. In section 4.1, we provide a design for the real structure model followed by a field analysis of the structure by the use of Maxwell equations. In subsection 4.2.2 and 4.2.3 we contrast the simulations results between the close ring and the split one, in order to explain the stopband observed in the split ring. Subsection 4.2.4 provides a detailed explanation for the observations made. Subsection 4.2.5 discusses the retrieval of the effective parameters of the structure, assuming an effective medium theory, and thereby compares the results to those of chapter 2 with transmission line loaded of lumped elements resonators.

In section 5, we conclude the thesis work, which is by no means exhaustive. We present our possible future work with applications to relevant topics of modern microwaves and wireless communications.

Chapter 2

Transmission Lines Modeling

2.1 Basic Transmission Lines Modeling

2.1.1 Real Transmission Lines

We start with a two-port description of a transmission line [19]:

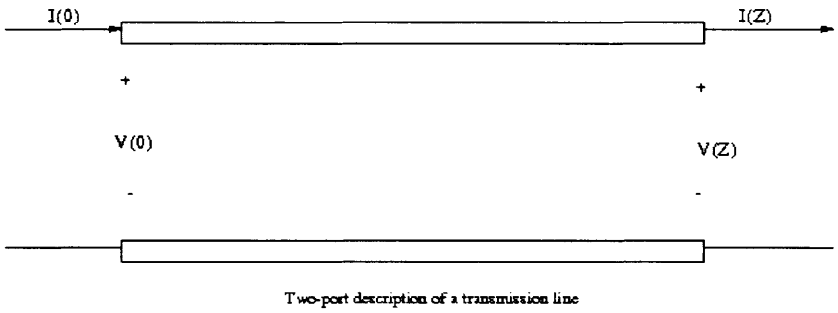

Figure 2.1.1 Two-port description of a transmission line.

The voltage $V(z)$ can be written in terms of the forward voltage V_+ and backward voltage V_- as follows:

$$\begin{aligned} V(z) &= V_+ \exp(-jkz) + V_- \exp(jkz) \\ I(z) &= Y_0 \left(V_+ \exp(-jkz) - V_- \exp(jkz) \right) \end{aligned} \qquad (2.1.1)$$

Solving the above set of equations for V_+ and V_- at $z = 0 \Rightarrow$

$$\begin{bmatrix} V(z) \\ I(z) \end{bmatrix} = \begin{bmatrix} \cos(kz) & -jZ_0 \sin(kz) \\ -jY_0 \sin(kz) & \cos(kz) \end{bmatrix} \begin{bmatrix} V(0) \\ I(0) \end{bmatrix} \qquad (2.1.2)$$

which is the inverse of the propagation matrix.

2.1.2 Lumped Elements Transmission Lines

In the same manner we can use the lumped element model to approximate the continuous transmission line by using its distributed parameters. Recall that Maxwell equations applied to a parallel-plate transmission line reduce to the following pair of equations:

$$\begin{aligned} \frac{\partial}{\partial z}V(z,t) &= -L\frac{\partial}{\partial t}I(z,t) \\ \frac{\partial}{\partial z}I(z,t) &= -C\frac{\partial}{\partial t}V(z,t) \end{aligned} \qquad (2.1.3)$$

Where L (inductance per unit length) and C (capacitance per unit length) are known as circuit parameters. But since $V(z,t)$ and $I(z,t)$ are eigenfunctions of frequency ω the pair of equations (2.1.3) becomes:

$$\frac{\partial}{\partial z}V(z,t) = -j\omega LI(z) \qquad (2.1.4)$$

$$\frac{\partial}{\partial z}V(z,t) = -j\omega CV(z) \qquad (2.1.5)$$

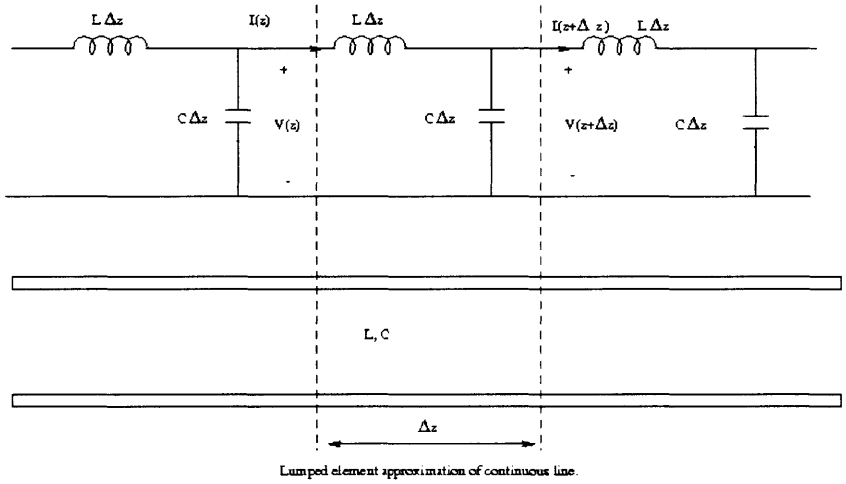

Figure 2.1.2 Lumped element approximation of continuous transmission line.

2.2 Periodically Loaded Transmission Lines Analysis Using Transfer Matrices

Consider the following periodically loaded transmission line

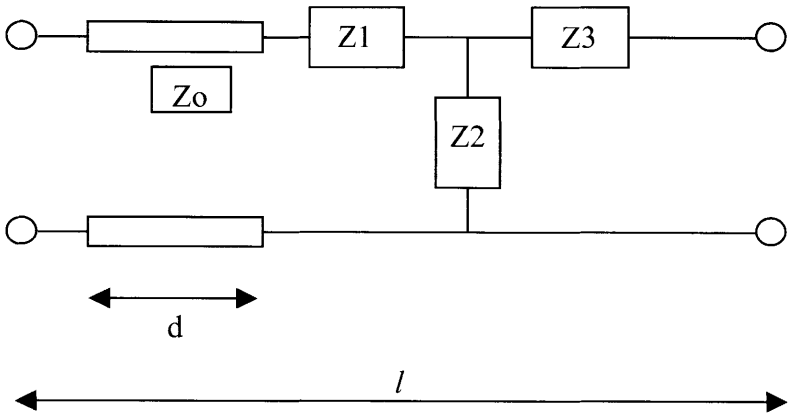

Figure 2.2.1 One period of a transmission line loaded with T networks loads.

Recall the ABCD matrix, namely propagation matrix relates the voltage and current of port 1 to the voltage and current of port 2 by the following relation [29]:

$$\begin{bmatrix} V_1 \\ I_1 \end{bmatrix} = \begin{bmatrix} A & B \\ C & D \end{bmatrix} \begin{bmatrix} V_2 \\ -I_2 \end{bmatrix} \quad (2.2.1)$$

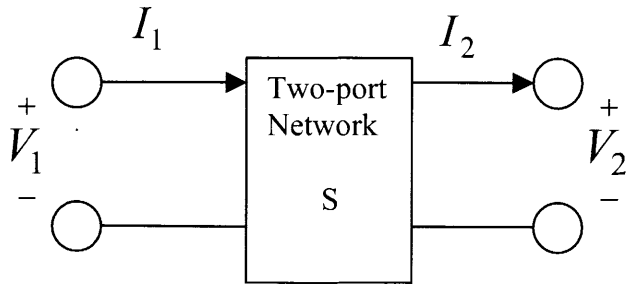

Figure 2.2.2 Two-port network.

The Transfer Matrix relates the voltage and current of Port1 to those of Port 2. The following relation relates the Transfer Matrix and the S parameters:

$$\overline{\overline{T}} = \begin{bmatrix} A & B \\ C & D \end{bmatrix}; \overline{\overline{S}} = \begin{bmatrix} S_{11} & S_{12} \\ S_{21} & S_{22} \end{bmatrix} \quad (2.2.2)$$

$$\overline{\overline{S}} = \frac{1}{D_a}\begin{bmatrix} A + \frac{B}{Z_O} - CZ_O - D & 2(AD - BC) \\ 2 & -A + \frac{B}{Z_O} - CZ_O + D \end{bmatrix} \; ; \; D_a = A + \frac{B}{Z_O} + CZ_O + D \quad (2.2.3)$$

Similarly we can relate the Z parameters to those of the transfer matrix.

$$\overline{\overline{Z}} = \begin{bmatrix} Z_{11} & Z_{12} \\ Z_{21} & Z_{22} \end{bmatrix} = \frac{1}{C}\begin{bmatrix} A & AD - BC \\ 1 & D \end{bmatrix} \quad (2.2.4)$$

$$\overline{\overline{T}} = \begin{bmatrix} A & B \\ C & D \end{bmatrix} = \frac{1}{Z_{21}}\begin{bmatrix} Z_{11} & Z_{11}Z_{22} - Z_{12}Z_{21} \\ 1 & Z_{22} \end{bmatrix} \quad (2.2.5)$$

Using the cascaded model for the loaded transmission line and treating the n^{th} cell as a two ports network and without loss of generality we can set l = d.

$$\begin{bmatrix} A & B \\ C & D \end{bmatrix} = \begin{bmatrix} \cos(kd) & jZ_0 \sin(kd) \\ jY_0 \sin(kd) & \cos(kd) \end{bmatrix}\begin{bmatrix} 1 & Z_1 \\ 0 & 1 \end{bmatrix}\begin{bmatrix} 1 & 0 \\ Y_2 & 1 \end{bmatrix}\begin{bmatrix} 1 & Z_3 \\ 0 & 1 \end{bmatrix} \quad (2.2.6)$$

$$\text{with } Y_2 = \frac{1}{Z_2}$$

Therefore the Dispersion relation in absence of the transmission line is:

$$2\cos\theta = 2 + \frac{Z_1 + Z3}{Z_2} \quad (2.2.7)$$

For the dispersion relation for the loaded line as shown in figure 2.2.1, we use equation (2.2.6),

$$A + \mathrm{D} = 2\cos\theta \quad (2.2.8)$$

The general dispersion relation for the loaded line is:

$$\cos\theta = \frac{1}{2}\left[(\cos kd)\left(2+\frac{Z_1}{Z_2}+\frac{Z_3}{Z_2}\right)+j\frac{Z_0}{Z_2}\sin kd+(jY_0\sin kd)\left(Z_1+Z_3+\frac{Z_1Z_3}{Z_2}\right)\right] \quad (2.2.9)$$

Similarly, from the S parameters we can derive the forward and backward normalized characteristic impedance of a unit cell at the reference planes defined for voltages and current according to the formula:

$$\overline{Z}_B^{\pm} = \frac{2B}{D-A\pm\sqrt{(A+D)^2-4}} \quad (2.2.10)$$

Where $\overline{Z}_B^{+}$ respectively ($\overline{Z}_B^{-}$) represent the forward normalized Bloch impedance respectively (backward Bloch impedance).

2.3 Derivation of Effective Parameters from a T/Pi Configuration Network Composed of Resonators

2.3.1 Transmission Line Loaded with Periodical T Bulk Insertions

Consider the network in Figure 2.3.1 below,

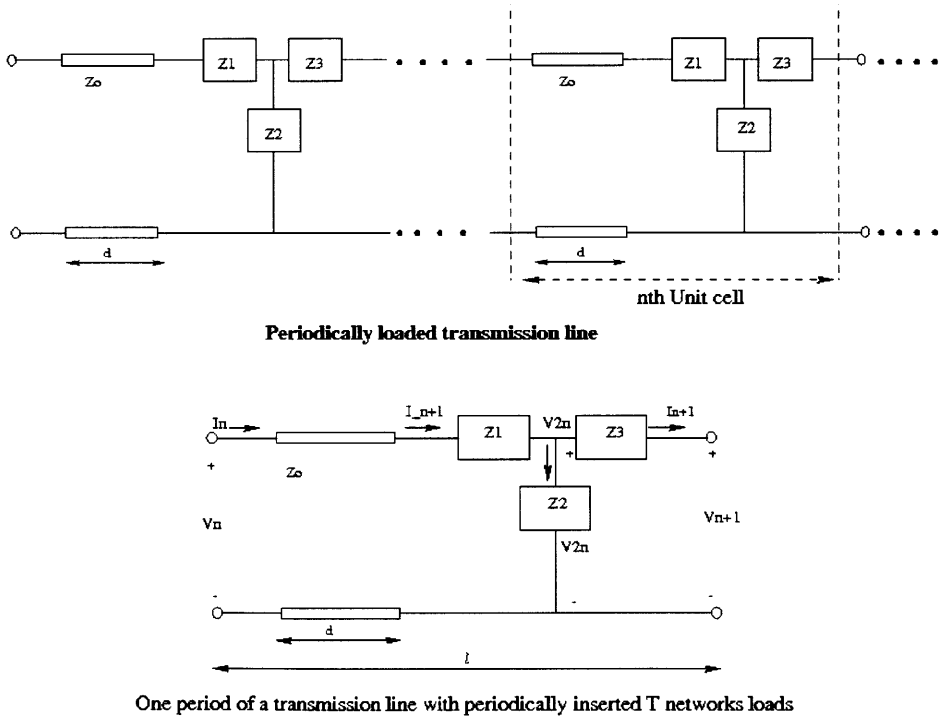

Figure 2.3.1 Transmission line loaded with periodical T networks loads.

KCL and KVL give:

$$I_{n+1} = I_n \exp(-j\theta) \quad (2.3.1)$$
$$V_{n+1} = V_n \exp(-j\theta) \quad (2.3.2)$$
$$\tilde{V}_{n+1} = V_n \cos(kl) - jZ_0 I_n \sin(kl) \quad (2.3.3)$$
$$\tilde{I}_{n+1} = -jY_0 V_n \sin(kl) + I_n \cos(kl) \quad (2.3.4)$$

Applying Kirchhoff's current and voltage law at node n_2 we obtain:

$$\tilde{I}_{n+1} = Y_2 V_{n2} + I_{n+1} \quad (2.3.5) \quad \text{With } Y_2 = \frac{1}{Z_2}$$

$$\tilde{V}_{n+1} - V_{n2} = Z_1 \tilde{I}_{n+1} \Rightarrow V_{n2} = \tilde{V}_{n+1} - Z_1 \tilde{I}_{n+1} \quad (2.3.6)$$

Similarly the current I_{n+1} can be expressed as:

$$I_{n+1} = \frac{V_{n2} - V_{n+1}}{Z_3} \Rightarrow V_{n2} - V_{n+1} = Z_3 I_{n+1} \quad (2.3.7)$$

Combining (2.3.5) and (2.3.6)

$$\Rightarrow \tilde{V}_{n+1} = Z_1 \tilde{I}_{n+1} + Z_3 I_{n+1} + V_{n+1} \quad (2.3.8)$$

Substituting equation (2.3.6) into (2.3.5)

$$\Rightarrow \tilde{I}_{n+1} = Y_2(\tilde{V}_{n+1} - Z_1 \tilde{I}_{n+1}) + I_{n+1}$$

Solving for $\tilde{I}_{n+1}$, we get:

$$\tilde{I}_{n+1} = \frac{Y_2 \tilde{V}_{n+1} + I_{n+1}}{1 + Y_2 Z_1} \quad (2.3.9)$$

Substituting (2.3.8) into (2.3.9)

$$\Rightarrow \tilde{I}_{n+1} = \frac{Y_2}{(1+Y_2Z_1)}\left(Z_1\tilde{I}_{n+1} + Z_3I_{n+1} + V_{n+1}\right) + \frac{1}{(1+Y_2Z_1)}I_{n+1}$$

$$\Rightarrow \tilde{I}_{n+1}\left(1 - \frac{Z_1Y_2}{(1+Y_2Z_1)}\right) = \left(\frac{Y_2}{1+Y_2Z_1}\right)\left(Z_3I_{n+1} + V_{n+1}\right) + \frac{1}{(1+Y_2Z_1)}I_{n+1}$$

$$\Rightarrow \tilde{I}_{n+1} = \left[Y_2\left(Z_3I_{n+1} + V_{n+1}\right) + I_{n+1}\right] \quad (2.3.10)$$

Substituting (2.3.10) into (2.3.8) leads to:

$$\tilde{V}_{n+1} = Z_1\left[Y_2\left(Z_3I_{n+1} + V_{n+1}\right) + I_{n+1}\right] + Z_3I_{n+1} + V_{n+1} \quad (2.3.11)$$

Substituting (2.3.1) and (2.3.2) into (2.3.11) and equating it with (2.3.3) $\Rightarrow$

$$\tilde{V}_{n+1} = \exp(-j\theta)\left\{Z_1\left[Y_2\left(Z_3I_n + V_n\right) + I_n\right] + Z_3I_n + V_n\right\} = V_n\cos(kl) - jZ_0I_n\sin(kl) \quad (2.3.12)$$

Similarly substituting (2.3.1) and (2.3.2) into (2.3.10) and equating it with (2.3.4), we obtain:

$$\tilde{I}_{n+1} = \exp(-j\theta)\left[Y_2\left(Z_3I_n + V_n\right) + I_n\right] = -jY_0V_n\sin(kl) + I_n\cos(kl) \quad (2.3.13)$$

$$\left(Z_1Y_2Z_3I_n + Z_1Y_2V_n + Z_1I_n + Z_3I_n + V_n\right)\exp(-j\theta) = V_n\cos(kl) - jZ_0I_n\sin(kl) \quad (2.3.14)$$

$$(Y_2Z_3I_n + Y_2V_n + I_n)\exp(-j\theta) = -jY_0V_n\sin(kl) + I_n\cos(kl) \quad (2.3.15)$$

Rearranging equations (2.3.14) and (2.3.15) leads to the following system of equations

$$\left\{\begin{array}{c} V_n\left[\left(Z_1Y_2+1\right)\exp(-j\theta)-\cos(kl)\right]=-I_n\left[jZ_0\sin(kl)+\left(Z_1Y_2Z_3+Z_3+Z_1\right)\exp(-j\theta)\right] (2.3.16) \\ V_n\left[jY_0\sin(kl)+\exp(-j\theta)Y_2\right]=I_n\left[\cos(kl)-\left(Y_2Z_3+1\right)\exp(-j\theta)\right] (2.3.17) \end{array}\right\}$$

Multiplying equations (2.3.16) by (2.3.17) sides by sides $\Rightarrow$

$$\frac{V_n^2}{I_n^2}=\frac{\left[jZ_0\sin(kl)+\left[Z_1+Z_3(Z_1Y_2+1)\right]\exp(-j\theta)\right]\left[(1+Y_2Z_3)\exp(-j\theta)-\cos(kl)\right]}{\left[jY_0\sin(kl)+Y_2\exp(-j\theta)\right]\left[(1+Y_2Z_1)\exp(-j\theta)-\cos(kl)\right]} \quad (2.3.18)$$

The impedance of the n^{th} unit cell is:

$$Z_n=\frac{V_n}{I_n}; (2.3.19)$$

$$Z_n=\sqrt{\frac{\left[jZ_0\sin(kl)+\left[Z_1+Z_3(Z_1Y_2+1)\right]\exp(-j\theta)\right]\left[(1+Y_2Z_3)\exp(-j\theta)-\cos(kl)\right]}{\left[jY_0\sin(kl)+Y_2\exp(-j\theta)\right]\left[(1+Y_2Z_1)\exp(-j\theta)-\cos(kl)\right]}} (2.3.20)$$

Similarly, to derive the Dispersion relation we make use of equations (2.3.16) and (2.3.17). This time by performing cross multiplication, we obtain:

$$\begin{aligned} &V_nI_n\left[\left(1+Z_1Y_2\right)\exp(-j\theta)-\cos(kl)\right]\left[\cos(kl)-\left(1+Y_2Z_3\right)\exp(-j\theta)\right]= \\ &-V_nI_n\left\{jZ_0\sin(kl)+\exp(-j\theta)\left[Z_3\left(1+Y_2Z_1\right)+Z_1\right]\right\}\left[jY_0\sin(kl)+Y_2\exp(-j\theta)\right] \end{aligned}$$

Simplifying by V_nI_n, will lead to:

$$\begin{aligned} &\left[\left(1+Z_1Y_2\right)\exp(-j\theta)-\cos(kl)\right]\left[\cos(kl)-\left(1+Y_2Z_3\right)\exp(-j\theta)\right]= \\ &-\left\{jZ_0\sin(kl)+\exp(-j\theta)\left[Z_3\left(1+Y_2Z_1\right)+Z_1\right]\right\}\left[jY_0\sin(kl)+Y_2\exp(-j\theta)\right] \end{aligned} \quad (2.3.21)$$

The Left Hand Side of equation (2.3.21)

$$LHS = (1+Z_1Y_2)\cos(kl)\exp(-j\theta) - (1+Y_2Z_3)(1+Z_1Y_2)\exp(-j2\theta) - \cos^2(kl) + (1+Z_3Y_2)\cos(kl)\exp(-j\theta)$$

and the Right Hand Side is:

$$RHS = -\left\{\begin{array}{l} -\sin^2(kl) + jY_0\sin(kl)\exp(-j\theta)\left[(1+Z_1Y_2)Z_3 + Z_1\right] + \\ jY_2Z_0\sin(kl)\exp(-j\theta) + Y_2\exp(-j2\theta)\left[(Z_1Y_2+1)Z_3 + Z_1\right] \end{array}\right\}$$

$$(1+Z_1Y_2)\cos(kl)\exp(-j\theta) - (1+Y_2Z_3)(1+Z_1Y_2) + (1+Y_2Z_3)\cos(kl)\exp(-j\theta) =$$
$$1 - jY_0\sin(kl)\left[(1+Y_2Z_1)Z_3 + Z_1\right]\exp(-j\theta) - jY_2Z_0\exp(-j\theta)\sin(kl) - Y_2\left[Z_1 + (1+Z_1Y_2)Z_3\right]\exp(-j\theta)$$

Multiplying the above equation by $\exp(j\theta) \Rightarrow$

$$(1+Z_1Y_2)\cos(kl) - (1+Z_3Y_2)(1+Z_1Y_2)\exp(-j\theta) + (1+Z_3Y_2)\cos(kl) = \exp(j\theta) +$$
$$-jY_0\sin(kl)\left[Z_1 + Z_3(1+Z_1Y_2)\right] - jY_2Z_0\sin(kl) - Y_2\left[Z_1 + (1+Z_1Y_2)Z_3\right]\exp(-j\theta)$$

$$\Updownarrow$$

$$\left((1+Z_1Y_2) + (1+Z_3Y_2)\right)\cos(kl) + \left\{jY_0\left[Z_1 + (1+Z_1Y_2)Z_3\right] + jY_2Z_0\right\}\sin(kl) = \exp(j\theta) +$$
$$\exp(-j\theta)\left\{-Y_2\left[Z_1 + (1+Z_1Y_2)Z_3\right] + (1+Z_3Y_2)(1+Z_1Y_2)\right\}$$

$$\Updownarrow$$

$$(2+Z_1Y_2+Y_2Z_3)\cos(kl) + j\sin(kl)\left\{Y_0\left[Z_1 + (1+Z_1Y_2)Z_3\right] + Y_2Z_0\right\} = \exp(j\theta) +$$
$$\exp(-j\theta)\left\{-Y_2Z_1 - Y_2Z_3 - Y_2^2Z_1Z_3 + 1 + Y_2Z_1 + Y_2Z_3 + Y_2^2Z_1Z_3\right\}$$

$$\Updownarrow$$

$$(2+Z_1Y_2+Y_2Z_3)\cos(kl) + j\sin(kl)\left\{Y_0\left[Z_1 + (1+Z_1Y_2)Z_3\right] + Y_2Z_0\right\} = \exp(j\theta) + \exp(-j\theta)$$

$$\Updownarrow$$

$$(2+Z_1Y_2+Y_2Z_3)\cos(kl) + j\sin(kl)\left\{Y_0\left[Z_1 + (1+Z_1Y_2)Z_3\right] + Y_2Z_0\right\} = 2\cos(\theta) \quad (2.3.22)$$

Hence the Dispersion relation is:

$$\cos(\theta)=\frac{1}{2}\left\{\left(2+Z_1Y_2+Y_2Z_3\right)\cos(kl)+j\sin(kl)\left\{Y_0\left[Z_1+\left(1+Z_1Y_2\right)Z_3\right]+Y_2Z_0\right\}\right\} \quad (2.3.23)$$

Notice that equation (2.3.23) and (2.2.9) are the same.

2.3.2 Transmission Line Loaded with Periodical Pi Bulk Insertions

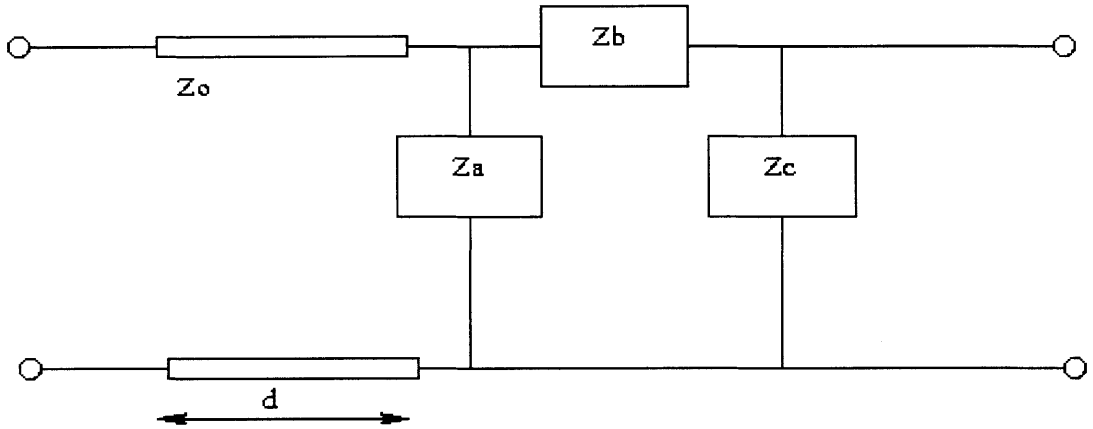

Figure 2.3.2 One unit cell of a transmission line loaded with Pi networks loads.

To derive the Impedance and Dispersion formulas for the Pi network we make use of the following transformations derived from elementary circuit theory [31].

Using elementary circuit theory [31] we can relate the impedances between the T configuration and the Pi configuration by the following relations:

$$\text{Pi to T configuration: } Z_1=\frac{Z_aZ_b}{Z_a+Z_b+Z_c},\quad Z_2=\frac{Z_aZ_c}{Z_a+Z_b+Z_c},\quad Z_3=\frac{Z_cZ_b}{Z_a+Z_b+Z_c} \quad (2.3.24)$$

And similarly we can get the impedances relations between the T to Pi configuration as followed:

$$Z_a = \frac{Z_1Z_2 + Z_1Z_3 + Z_2Z_3}{Z_3}$$
$$Z_b = \frac{Z_1Z_2 + Z_1Z_3 + Z_2Z_3}{Z_2} \qquad (2.3.25)$$
$$Z_c = \frac{Z_1Z_2 + Z_1Z_3 + Z_2Z_3}{Z_1}$$

Likewise, if we substitute equation (2.3.24) into equation (2.3.23) and after some calculations we obtain the dispersion relation for the π network as follow:

$$\cos(\theta) = \frac{1}{2}\left\{\left[2 + \frac{(Y_a + Y_c)}{Y_b}\right]\cos(kl) + j\sin(kl)\left[\frac{Y_0}{Y_b} + \frac{Y_c}{Y_0}\left(1 + Y_a\left(\frac{1}{Y_b} + \frac{1}{Y_c}\right)\right)\right]\right\} \qquad (2.3.26)$$

2.4 Analysis and Applications to Different Case Study

2.4.1 Unloaded Transmission Line

Consider the unloaded transmission line of figure 2.4.1 shown below. In all the following cases study, the length of the transmission line is taken to be d =1cm and with characteristic impedance $Z_0 = 50\Omega$.

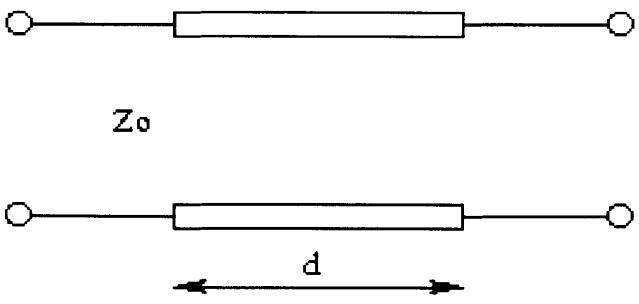

Figure 2.4.1 Unloaded transmission line of length d=1cm.

Letting $Z_1 = Z_3 = 0;$ and $Y_2 = 0;$

The Dispersion equation (2.2.9) $\Leftrightarrow$ $\cos\theta = \cos(kd)$ (2.4.1)

As a result, as the periodically loaded impedance approaches ∞, which is equivalent to the regular line with no insertions, we have $\cos\theta = \cos(kd) \Leftrightarrow \theta = kd$

For the periodical line, the values of $\theta = kd$ are confined by the limits 0 and π [30]

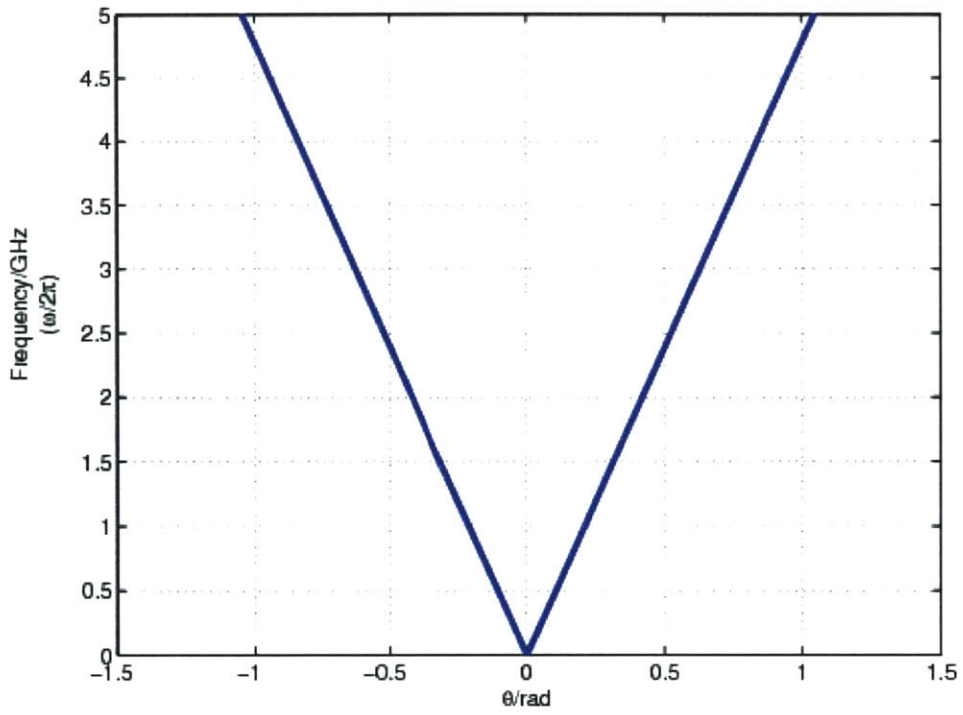

Figure 2.4.2 Dispersion curve for the unloaded transmission line of Figure 2.4.1.

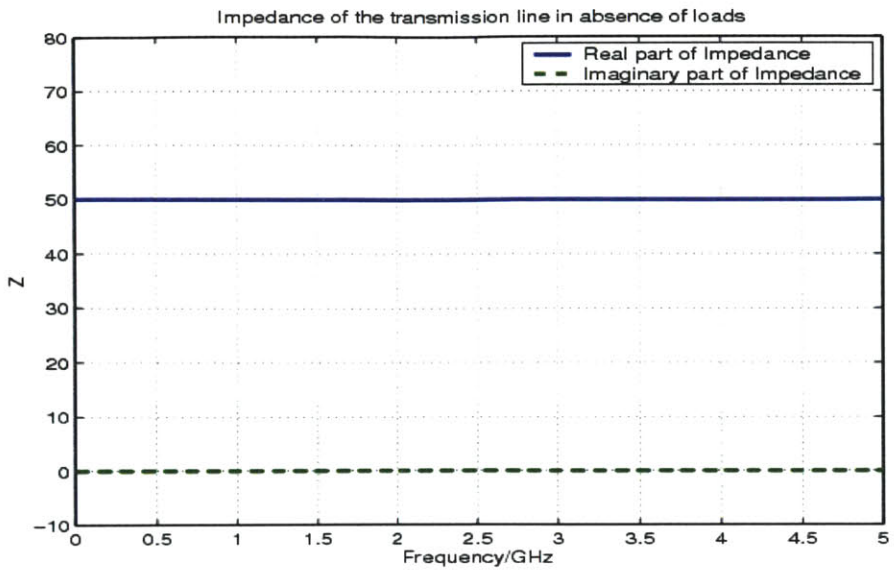

Figure 2.4.3 Impedance of the unloaded transmission line.

In absence of the loading, the impedance of the line should be equal to that of the intrinsic impedance Z_0, 50Ω as shown in the figure above.

2.4.2 Periodical Capacitively Loaded Transmission Lines

Consider a transmission line with lumped periodical capacitive insertions as shown below.

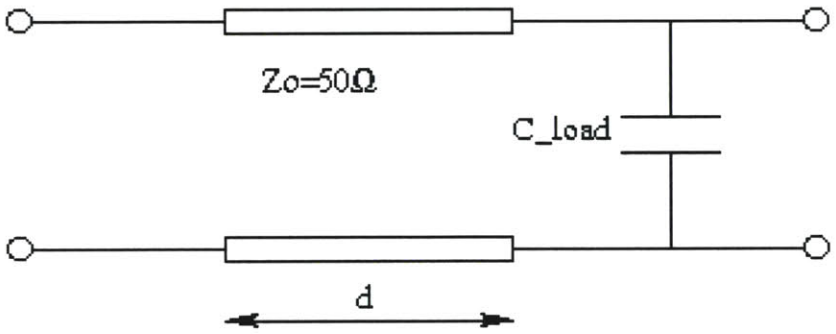

Figure 2.4.4 One period of a transmission line with periodical capacitive loads.

Letting $Z_1 = Z_3 = 0$; and $Y_2 = j\omega C_{load}$ $\Rightarrow$ (2.2.9) becomes:

$$\cos\theta = \cos(kd) - \frac{Z_0}{2}\omega C_{load}\sin(kd) \quad (2.4.2)$$

which is the dispersion relation for periodic capacitively loaded transmission lines.

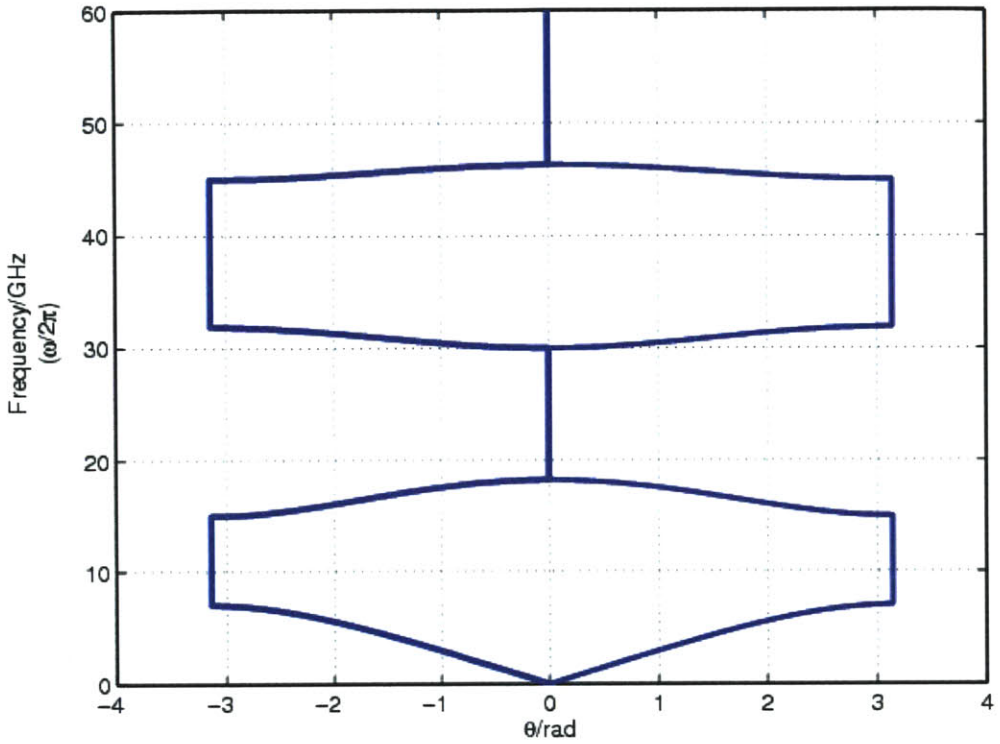

Figure 2.4.5 Typical dispersion curves for periodical capacitively loaded transmission lines with C_load=1pF and $Z_0 = 50\Omega$.

We observe a passband in the low frequency range and a stop-band in the high frequency range. This is because at low frequency the capacitor behaves as an open circuit with very large impedance, thereby passing all the low frequencies and attenuates the higher ones. Therefore the periodical capacitively loaded line behaves as a low pass filter.

From equation (2.4.2), it is obvious that when the magnitude of the right hand side is less than or equal to unity, we have a passband. Otherwise, the wave becomes evanescent and we have a stopband. As frequency (ω) increases, we can have an infinite number of passbands, but they become narrower and narrower.

2.4.3 Periodical Inductively Loaded Transmission Lines

Consider the transmission line of figure 2.4.6 below. Letting $Z_1 = Z_3 = 0$;

$$\text{and } Y_2 = \frac{1}{j\omega L_{load}} \Rightarrow (2.2.9) \text{ becomes:}$$

$$\cos\theta = \cos(kd) + \frac{Z_0}{2\omega L_{load}} \sin(kd) \quad (2.4.3)$$

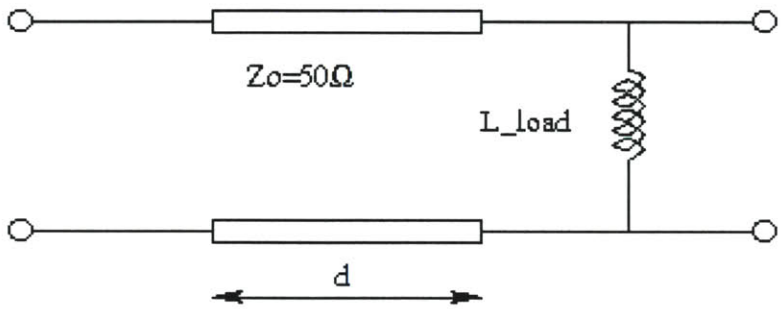

Figure 2.4.6 One period of a transmission line with periodical inductive loads.

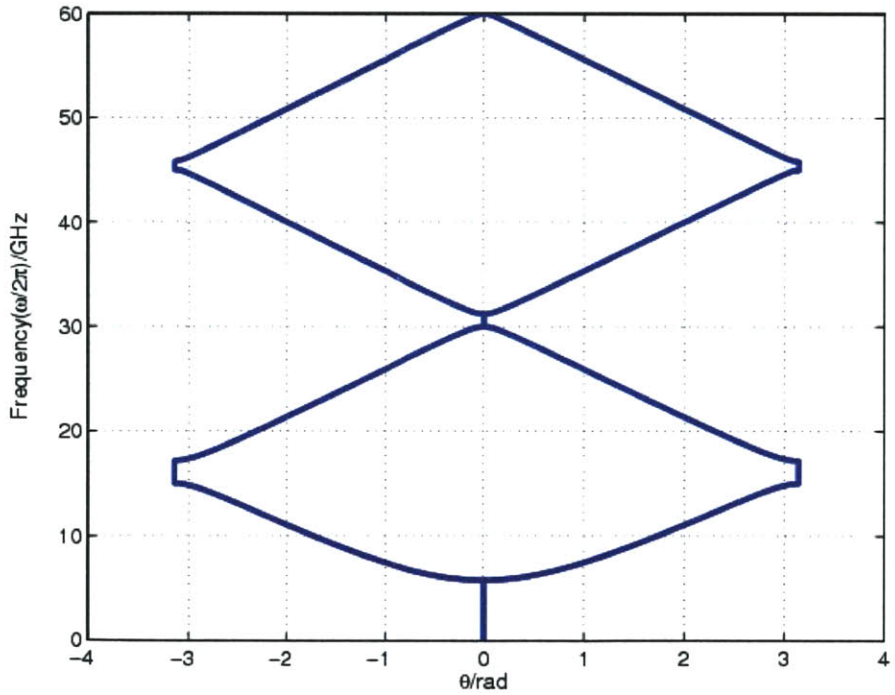

Figure 2.4.7 Typical dispersion curves for periodical inductively loaded transmission lines with L_load=1nH and $Z_0 = 50\Omega$.

We observe a low-frequency stop band due to very low impedances of the inductor. In low frequency, the inductor behaves as a short circuit. As a result, the periodical inductively loaded transmission line is a high pass filter in the lower part of the frequency spectrum. In a similar way, when the magnitude of the right hand side of equation (2.4.3) is less than or equal to unity, we have an infinite number of passbands but as frequency increases they become wider and wider. Otherwise the wave experience cut off and we have stopbands.

2.4.4 Periodical Transmission Line Loaded by a Series Inductance and Shunt Capacitance

Consider the transmission line with periodic loads composed of a series inductance and shunt capacitance as shown in figure 2.4.9 below.

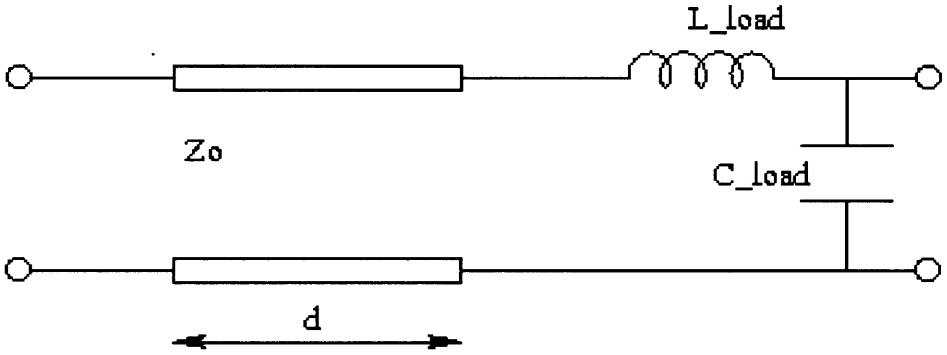

Figure 2.4.8 One unit cell of a Transmission line loaded with series inductance and shunt capacitance with Zo=50Ω, L_load=1nH, and C_load=1pF.

Letting $Z_3 = 0$; $Z_1 = j\omega L_{load}$ and $Y_2 = j\omega C_{load}$ $\Rightarrow$(2.2.9) becomes:

$$\cos\theta = \frac{1}{2}\left[\left(2-\omega^2 L_{load}C_{load}\right)\cos(kd) - \omega\left(Z_0 C_{load} + Y_0 L_{load}\right)\sin(kd)\right] \quad (2.4.4)$$

The above equation represents the dispersion relation for Figure 2.4.8.

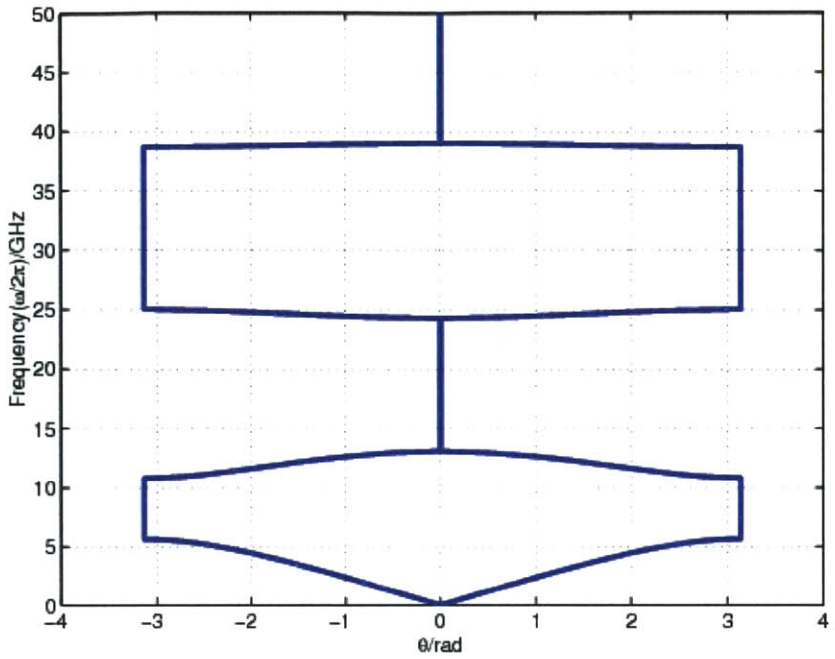

Figure 2.4.9 Dispersion curve for Figure 2.4.8.

2.4.5 Periodical Transmission Line Loaded by a Series Capacitance and Shunt Inductance

Consider the transmission line with periodic loads composed of a series capacitance and shunt inductance as shown in figure 2.4.10 below.

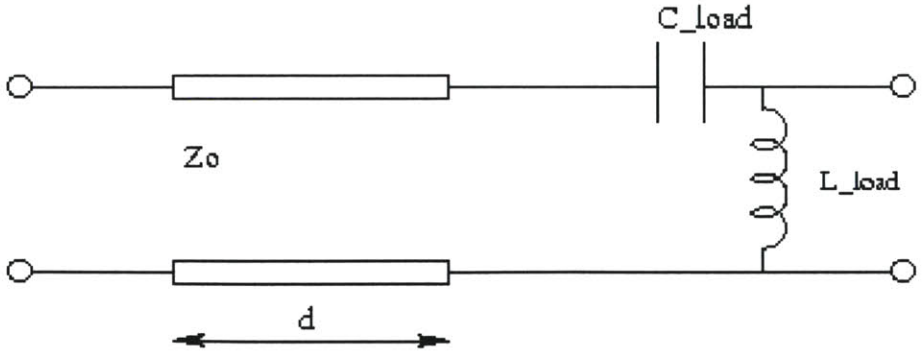

Figure 2.4.10 One unit cell of a Transmission line loaded with series capacitance and shunt inductance with Zo=50Ω, L_load=1nH, and C_load=1pF.

Letting $Z_3 = 0;\ Z_1 = \dfrac{1}{j\omega C_{load}}$ and $Y_2 = \dfrac{1}{j\omega L_{load}} \Rightarrow$ (2.2.9) becomes:

$$\cos\theta = \frac{\left(\left(2\omega^2 L_{load}C_{load} - 1\right)\cos(kd) + \omega\left(Y_0 L_{load} + Z_0 C_{load}\right)\sin(kd)\right)}{2\omega^2 L_{load}C_{load}} \quad (2.4.5)$$

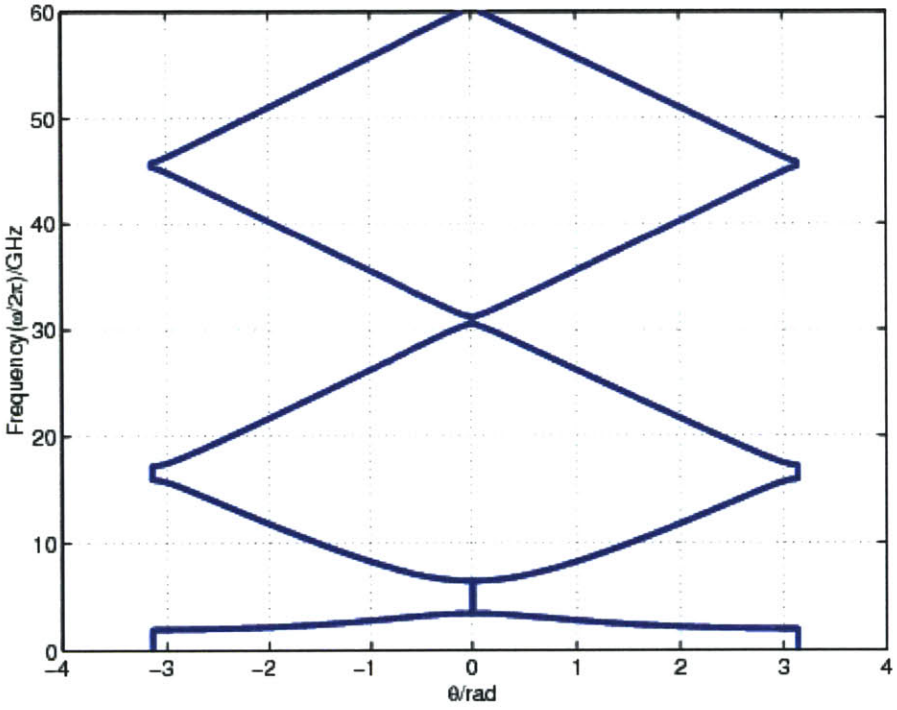

Figure 2.4.11 Dispersion curve for Figure 2.4.10.

The phase velocity $V_p = \dfrac{\omega}{k_{eff}}$ and $\theta = k_{eff}d \Rightarrow V_p = \dfrac{\omega d}{\theta}$

$$V_p = \frac{\omega d}{a\cos\left(\dfrac{\left(\left(2\omega^2 L_{load}C_{load} - 1\right)\cos(kd) + \omega\left(Y_0 L_{load} + Z_0 C_{load}\right)\sin(kd)\right)}{2\omega^2 L_{load}C_{load}}\right)} \quad (2.4.6)$$

and the group velocity $\vec{V}_g = \nabla_{\vec{k}}\omega \Leftrightarrow \vec{V}_g = \dfrac{1}{\dfrac{\partial k_{eff}}{\partial\omega}}$ (2.4.7)

To better understand the concept of left-handedness, let us look at the plots of both phase and group velocities versus frequency. In order to do this we need to distinguish between the following two cases:

2.4.5-a In Absence of Transmission Line

The dispersion relation is as followed:

$$\cos\theta = \frac{2\omega^2 L_{load} C_{load} - 1}{2\omega^2 L_{load} C_{load}} \qquad (2.4.8)$$

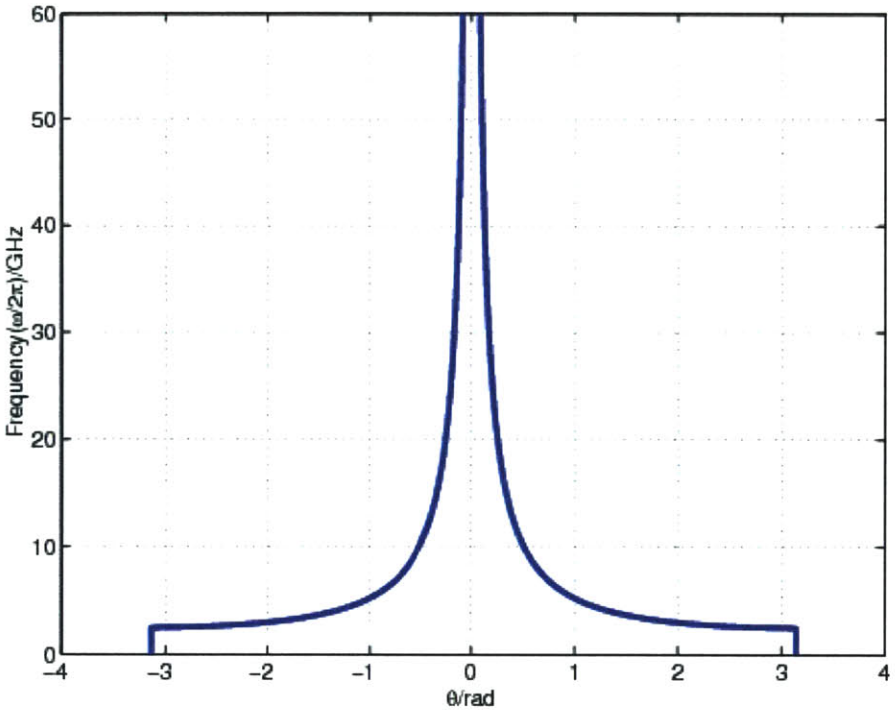

Figure 2.4.12 Dispersion curve for the structure of figure 2.4.10 in absence of the transmission line.

We observe a negative refraction from 2.46 GHz to 60 GHz, which means that the group velocity is negative and is verified in the plot below.

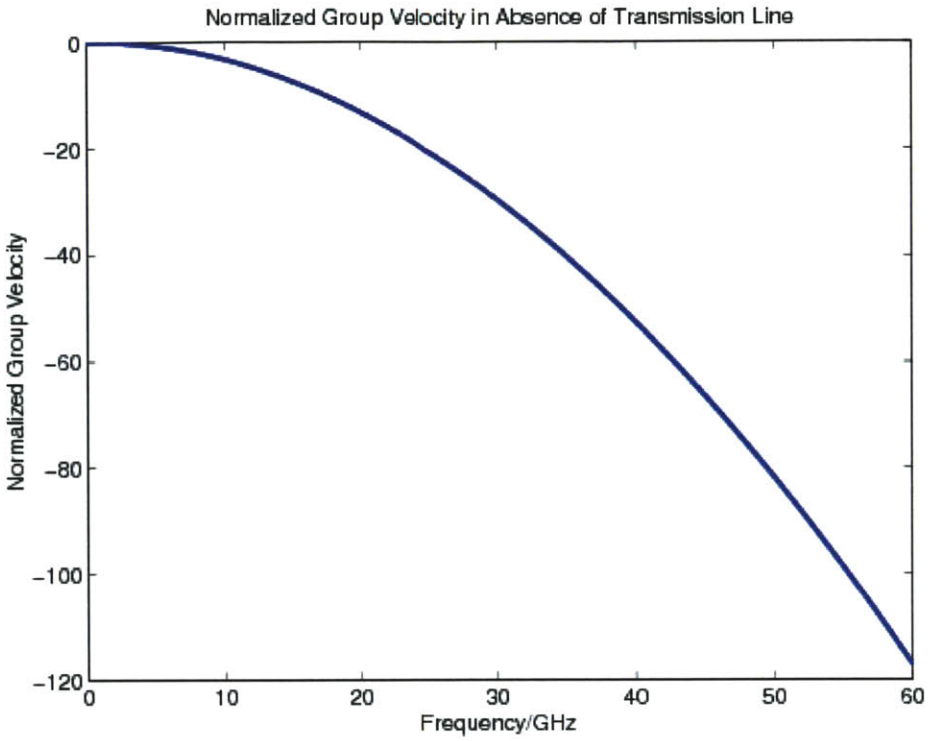

Figure 2.4.13 Group velocity for the structure of figure 2.4.10 without the transmission line.

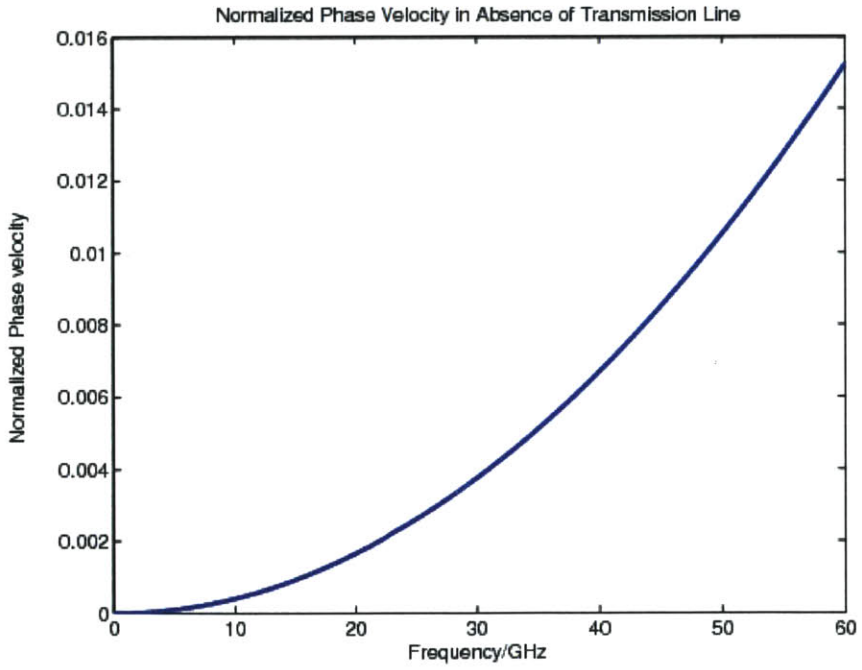

Figure 2.4.14 Phase velocity for the structure of figure 2.4.10 without the transmission line.

As seen above in figures 2.4.13 and 2.4.14, it is obvious that the group velocity is greater than the speed of light c whereas the phase velocity is smaller. Therefore, this is not a physical system and it does justify the use of transmission line. It is important to know all the information pertaining to the group velocity since the wave propagation and direction are determined by the group velocity rather than the phase velocity [32].

2.4.5-b In Presence of Transmission Line

In presence of the transmission line the dispersion curve is the same as that of figure 2.4.11.

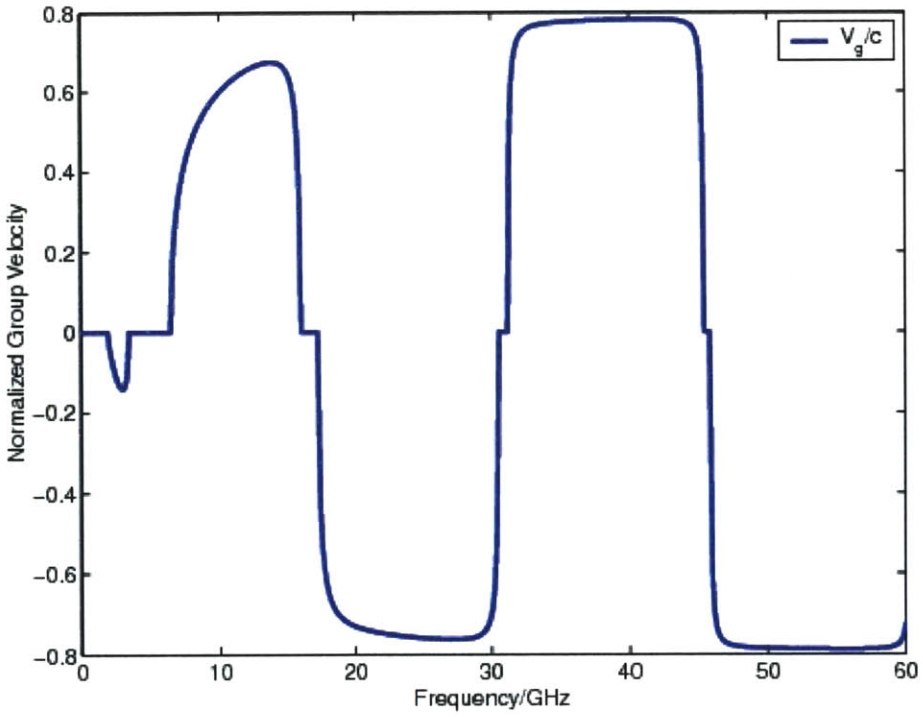

Figure 2.4.15 Group velocity for the structure of figure 2.4.10.

We notice that the group velocity is negative for $\frac{\omega}{2\pi} < 2.7GHz$ and also that the group velocity is always less than the speed of light c.

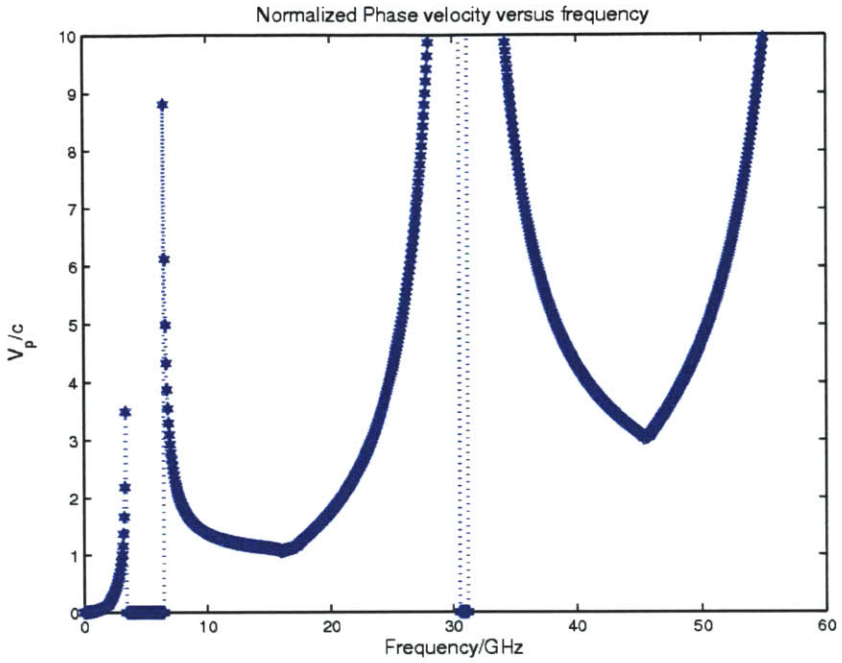

Figure 2.4.16 Normalized phase velocity for the structure shown in figure 2.4.10.

Contrary to the group velocity, the phase velocity is greater than the speed of light in a wide band of frequency and the normalized value is greater than 1. It becomes zero between 3.4- 6.4 GHz, and between 30.5- 31.2 GHz. It becomes infinity at the reflection point 2.7 GHz.

2.4.6 Periodical Transmission Line Loaded by a Resonant Parallel Connection of a Capacitance and Inductance

Consider a transmission line loaded by a resonant parallel connection of figure 2.4.17:

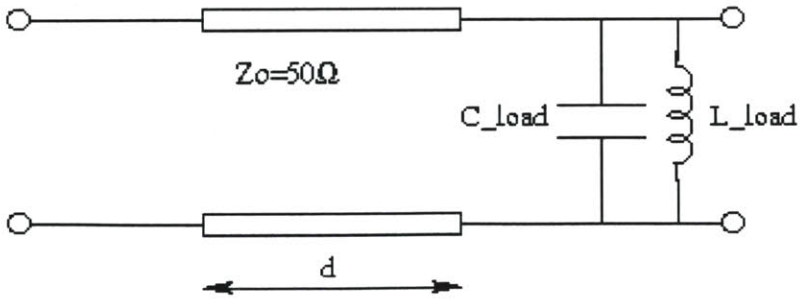

Figure 2.4.17 One period of a transmission line loaded by a resonant parallel load.

Letting $Z_1 = Z_3 = 0$; and $Y_2 = j\omega C_{load} + \dfrac{1}{j\omega L_{load}} \Rightarrow$ (2.2.9) becomes:

$$\cos\theta = \cos(kd) - \frac{Z_0}{2}\left(\omega C_{load} - \frac{1}{\omega L_{load}}\right)\sin(kd) \quad (2.4.9)$$

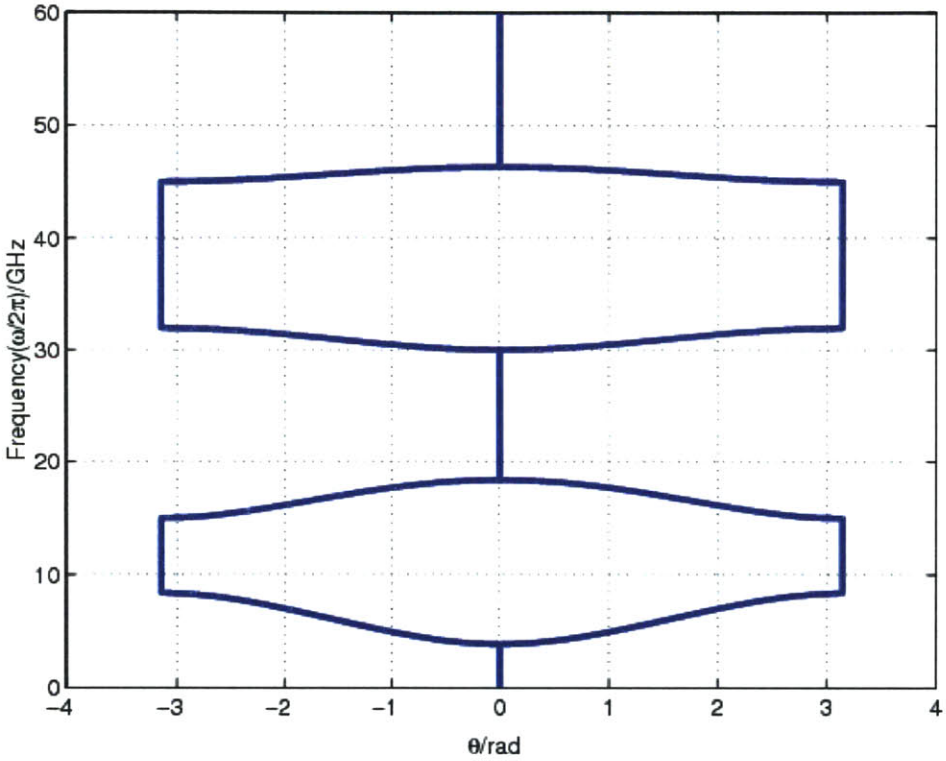

Figure 2.4.18 Dispersion curve for a periodical transmission line loaded with a resonant parallel connection of an inductance and capacitance.

At lower frequencies, the inductance of the parallel resonant connection dominates; therefore the periodical transmission line loaded by a parallel connection behave as a high pass filter in the lower end of the frequency spectrum. At higher frequencies however, the capacitance dominates, and the overall resonant parallel connection behaves as a low pass filter. The resonant frequency of the connection is found to be $f_0 = 5.04GHz$ for L_load=1nH and C_load=1pF.

2.4.7 Periodical Transmission Line Loaded by a Series Capacitance and Inductance

Consider the transmission line shown in figure 2.4.19 below:

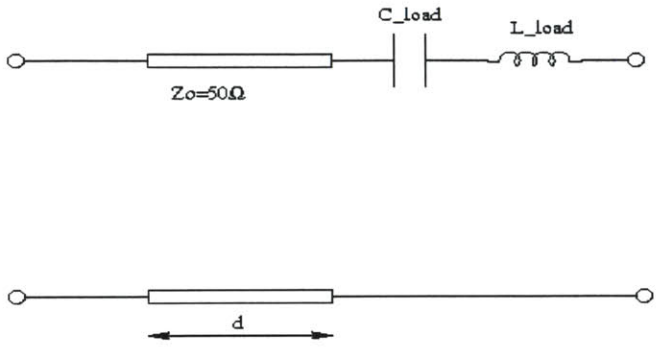

Figure 2.4.19 One unit cell of a Transmission line loaded with series capacitance and inductance with Zo=50Ω, L_load=1nH, and C_load=1pF.

Letting $Z_1 = \frac{1}{j\omega C_{load}} + j\omega L_{load}$; $Z_3 = 0$ and $Y_2 = 0$ in equation (2.2.9), the dispersion relation is:

$$\cos\theta = \frac{1}{2}\left(2\cos(kd) - \frac{jY_0\left(1-\omega^2 L_{load}C_{load}\right)\sin(kd)}{\omega C_{load}}\right) \quad (2.4.10)$$

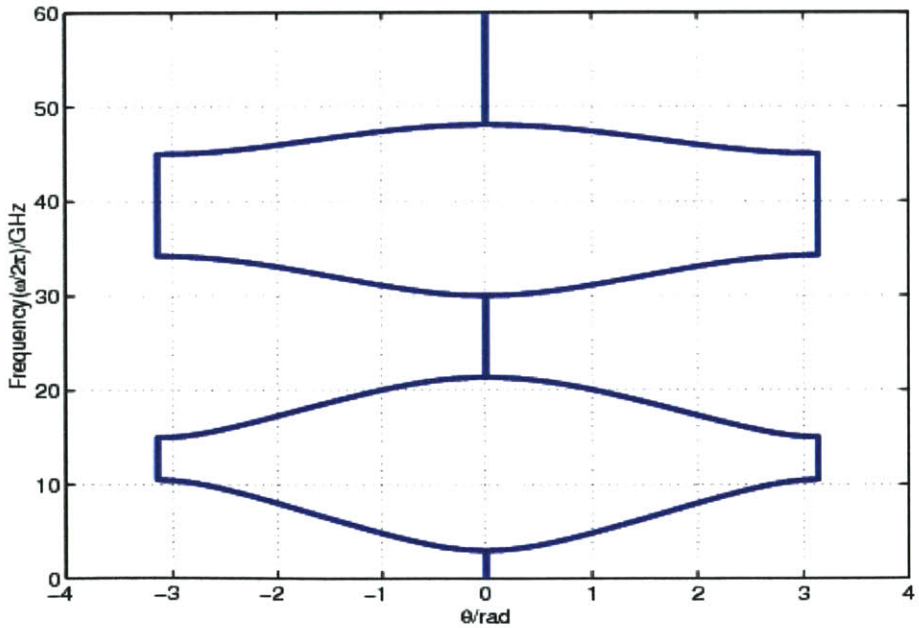

Figure 2.4.20 Typical dispersion curve for the structure shown in figure 2.4.19.

The structures shown in figures 2.4.17 and 2.4.19 are equivalent except that the second passband of the structure shown in figure 2.4.19 is wider.

2.4.8 Periodical Transmission Line Loaded by a Resonant Series Connection of a Capacitance and Inductance

Consider a transmission line loaded by a series connection of figure 2.4.21 below.

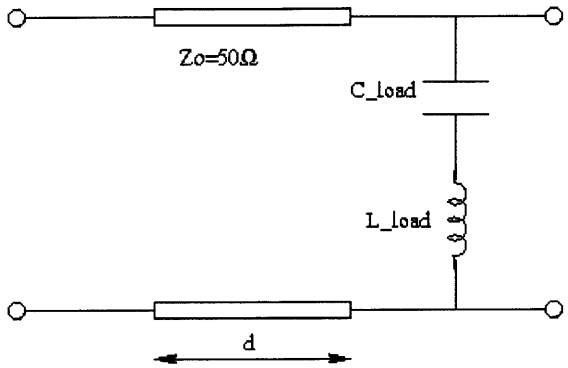

Figure 2.4.21 One period of a transmission line with a resonant series connection with L_load=1nH and C_load=1pF.

Letting $Z_1 = Z_3 = 0$; and $Y_2 = \dfrac{1}{\left(\dfrac{1}{j\omega C_{load}} + j\omega L_{load}\right)} \Rightarrow$ (2.2.9) becomes:

Thus the dispersion relation is $\cos\theta = \cos(kd) - \dfrac{Z_0}{2}\left(\dfrac{\omega C_{load}}{1-\omega^2 L_{load} C_{load}}\right)\sin(kd)$ (2.4.11)

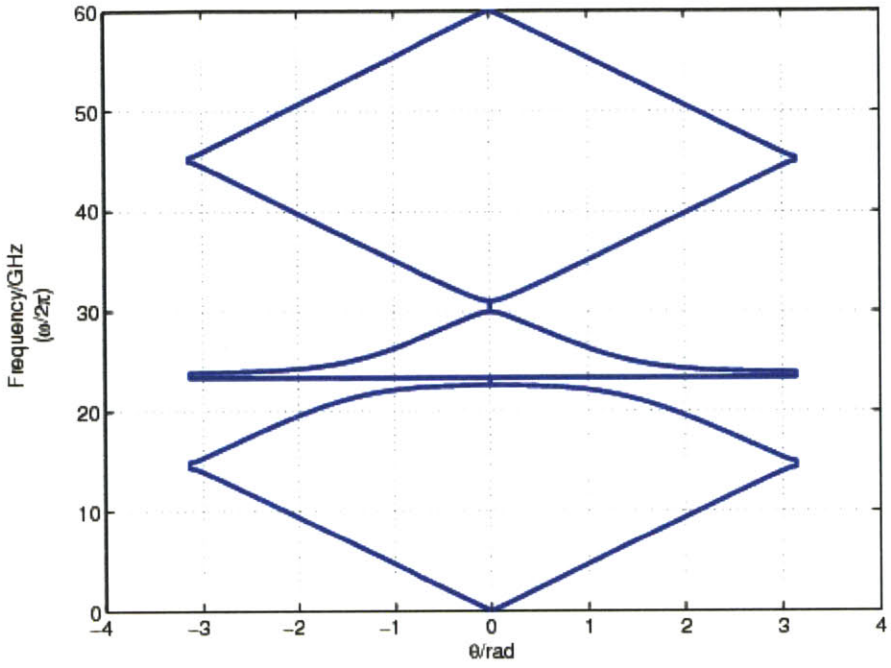

Figure 2.4.22 Dispersion curve for a periodical transmission line loaded with a resonant series connection of an inductance and capacitance of figure 2.4.21 with L_load=2.61nH and C_load=0.017pF.

Using the same analogy, in the series connection on the other hand, the capacitance dominates at low frequencies and we observe a pass band. As a result, the periodical transmission line loaded by a series resonant connection behaves as a capacitor.

At higher frequencies however, the inductor dominates and the load behaves as an inductor. It is of particular interest to also plot the S-parameters for the resonant structure of figure 2.4.21. From the ABCD matrix, we can derive the S parameters by using the appropriate conversion between two-port network parameters [34].

$$S_{11} = \frac{A + B/Z_0 - CZ_0 - D}{A + B/Z_0 + CZ_0 + D};\ S_{21} = \frac{2}{A + B/Z_0 + CZ_0 + D};$$
$$S_{22} = \frac{-A + B/Z_0 - CZ_0 + D}{A + B/Z_0 + CZ_0 + D};\ S_{12} = \frac{2(AD - BC)}{A + B/Z_0 + CZ_0 + D}; \qquad (2.4.12)$$

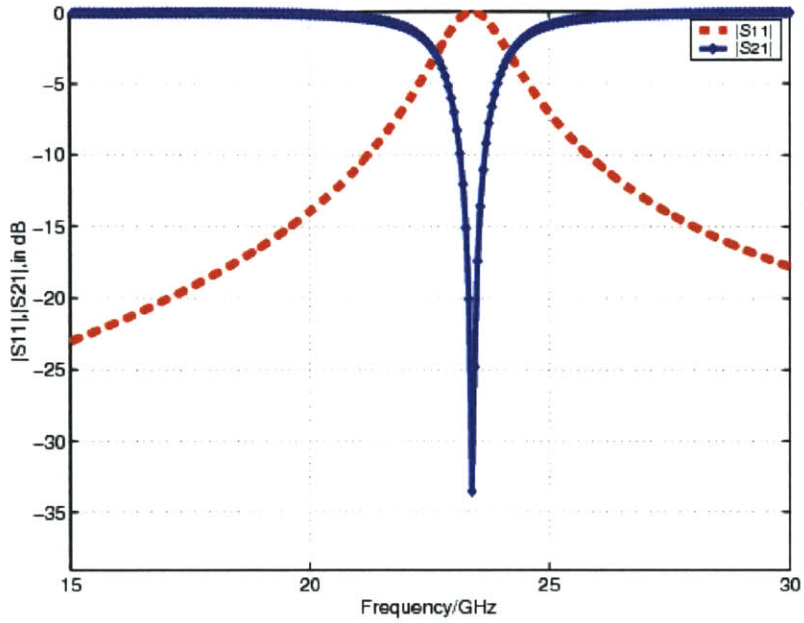

Figure 2.4.23 S-parameters for the structure of Figure 2.4.21 with L_load=2.61nH and C_load=0.01pF with a stopband at $f_0 = 23.4GHz$

From the S-parameters and the impedance Z, we calculate the index of refraction using the following equation:

$$n = \frac{c}{v_{phase}} = \frac{\theta}{\omega d} c \qquad (2.4.13)$$

$$\text{with} \quad \theta = k_{eff} d \quad (2.4.14)$$

From the above equations we can retrieve the per unit length inductance (L'= μ_{eff}) respectively the per unit length capacitance (C'= ε_{eff}) according to:

$$\mu_{eff} = \frac{k_{eff} Z_B^+}{\omega} \qquad (2.4.15)$$

$$\varepsilon_{eff} = \frac{k_{eff}}{\omega Z_B^+} \qquad (2.4.16)$$

$$\text{with} \quad \overline{Z}_B^+ = \frac{2B}{D - A + \sqrt{(A+D)^2 - 4}} \qquad (2.4.17)$$

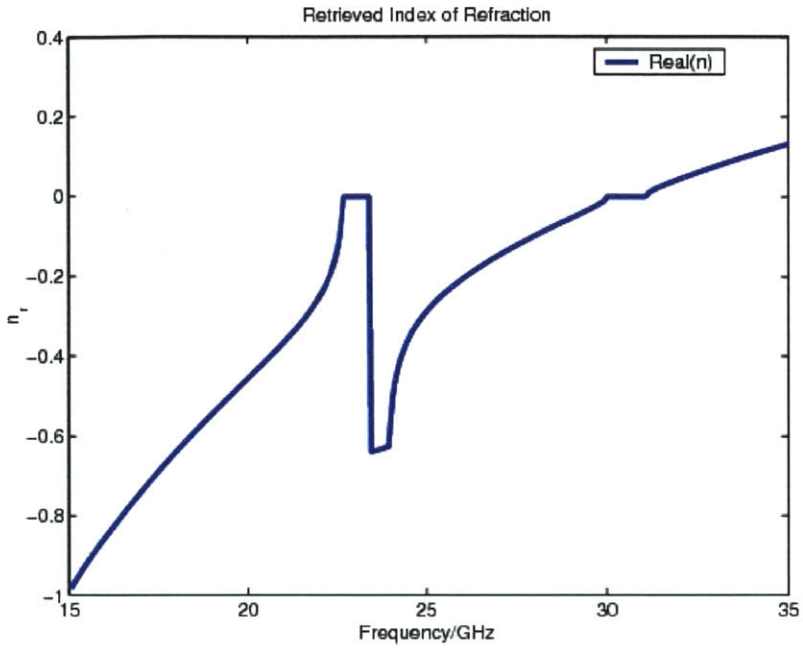

Figure 2.4.24 Real part of the index of refraction for the structure shown in figure 2.4.21.

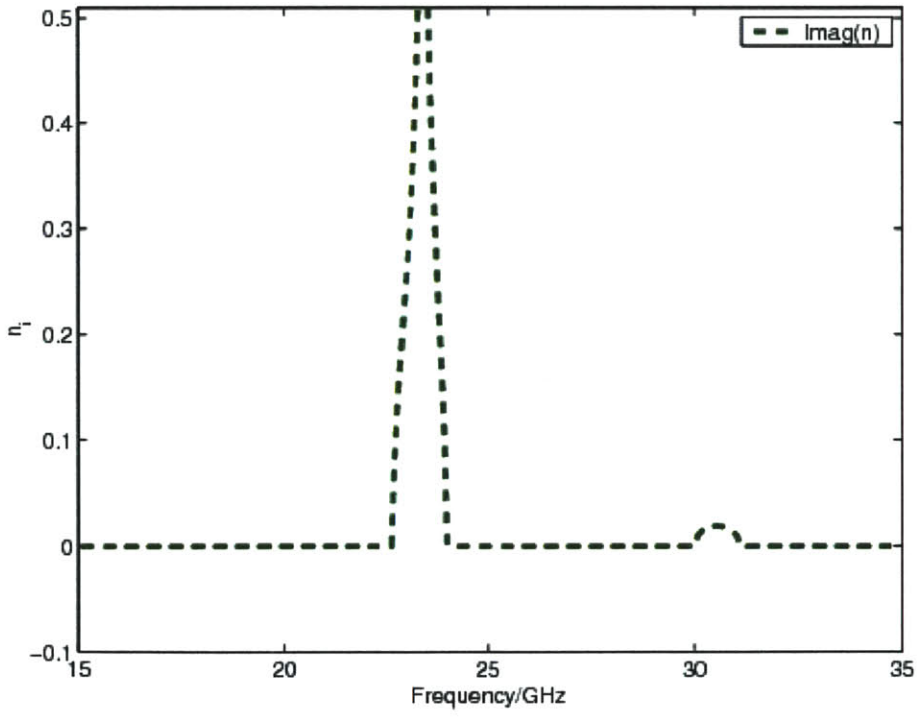

Figure 2.4.25 Imaginary part of the index of refraction for the structure shown in figure 2.4.21.

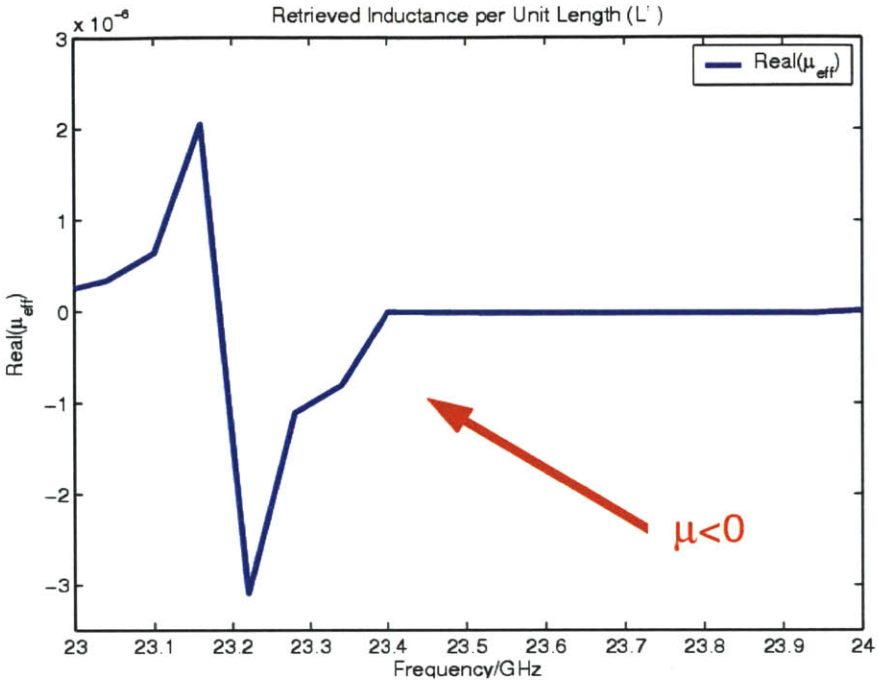

Figure 2.4.26 Real part of the inductance per unit length L' of the effective line shown in figure 2.4.21.

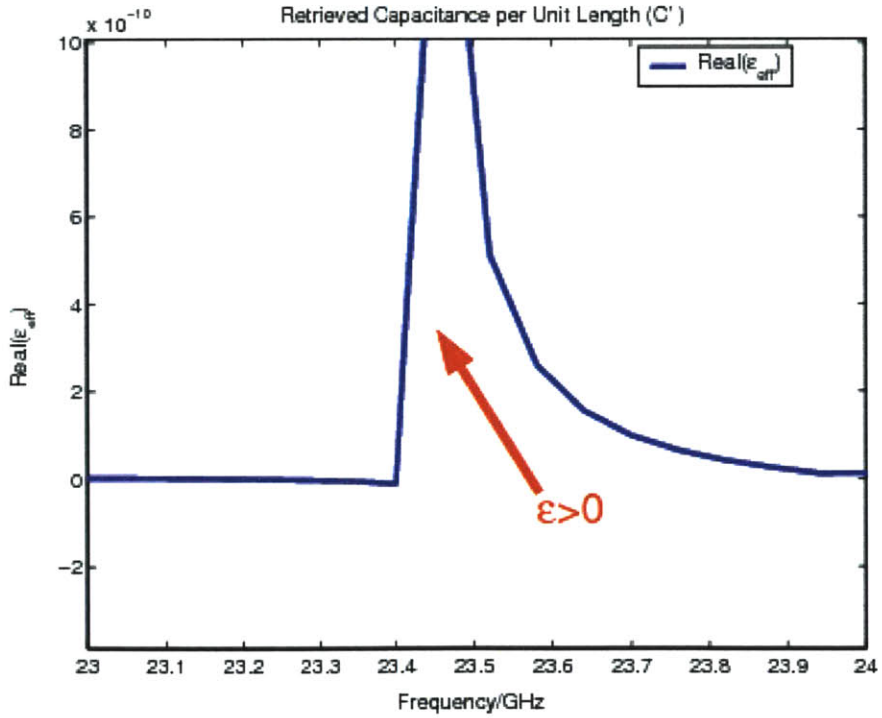

Figure 2.4.27 Real part of the capacitance per unit length C' of the effective line shown in figure 2.4.21.

2.4.9 Periodical Transmission Line Loaded by a Shunt Capacitance and Inductance in Series

Consider the transmission line of figure 2.4.29 shown below. Again by using the same procedures, we can derive the dispersion relation by letting:

$Y_2 = 0;\ Z_3 = 0;$ and $Z_1 = \dfrac{1}{j\omega C_{load} + \dfrac{1}{j\omega L_{load}}}$; in equation (2.2.9), the dispersion relation is:

$$\cos\theta = \frac{1}{2}\left(2\cos(kd) - \frac{Y_0 \omega L_{load} \sin(kd)}{1-\omega^2 L_{load} C_{load}}\right) \quad (2.4.18)$$

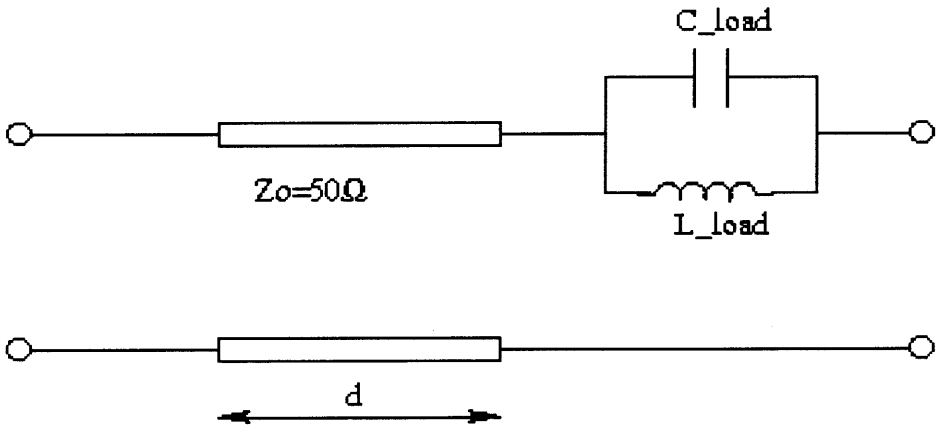

Figure 2.4.28 One period of a transmission line series loaded with a shunt inductance and capacitance with Zo=50Ω , L_load=1nH, and C_load=1pF.

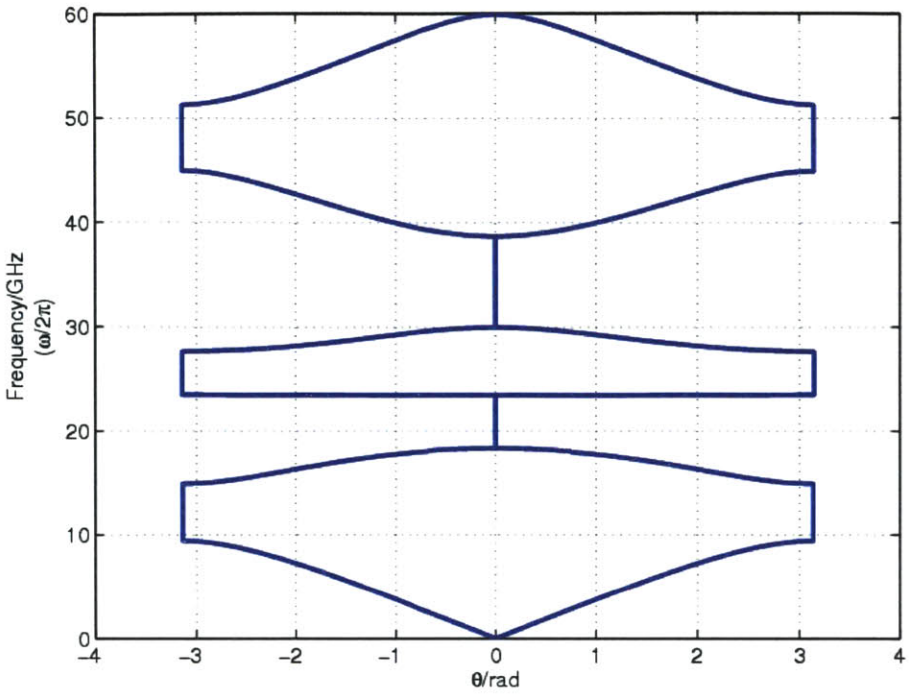

Figure 2.4.29 Dispersion curve of the structure shown in figure 2.4.28 with L_Load=.92nH and C_Load=.05pF.

Since the structure exhibits a resonant frequency at 23. 4 GHz, it is important for us to plot its S parameters, which will be very useful in determining the effective parameters of the structure in the subsequent chapters.

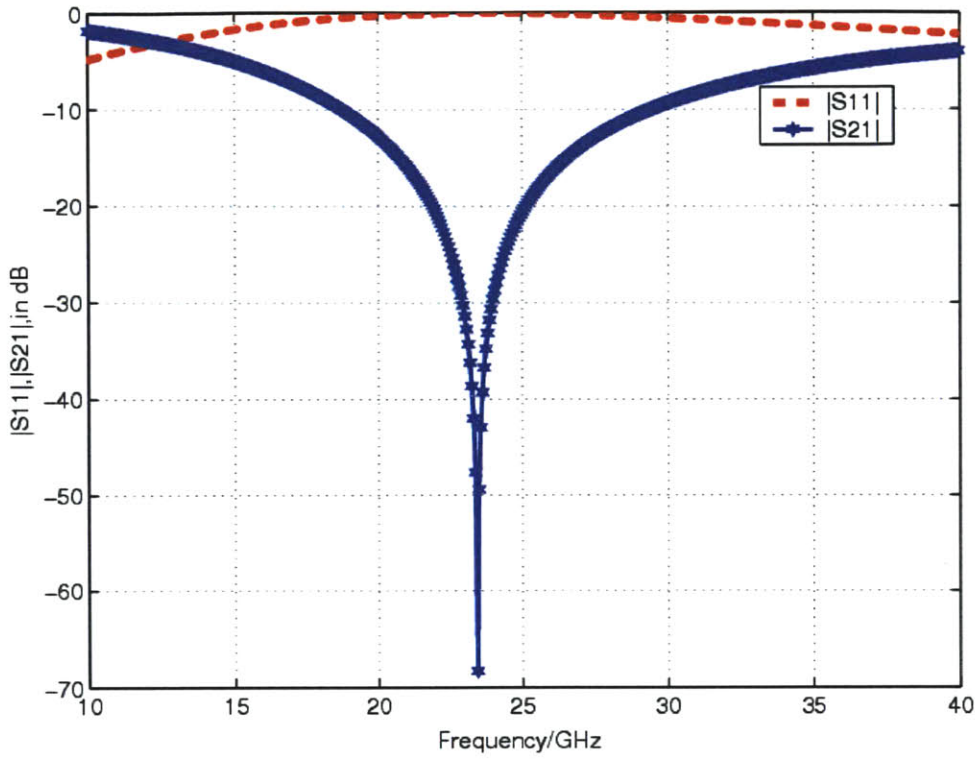

Figure 2.4.30 S-parameters for the structure shown in figure 2.4.28.

Again we notice a stopband at 23.4 GHz, which undoubtedly establishes the equivalence between the structures in figure 2.4.21 and the one in figure 2.4.28. The two cases are dual topology of each other. Because of fundamental limit in the ring design, considerations such as losses, quality factor and bandwidth, will be the determining factors in choosing the correct model for our resonator.

Chapter 3

Ring Designs and Analysis

In this chapter, we present the methodology of the ring structures, as well as numerical simulations of several designs.

3.1 Analysis Methodology

The methodology can be summarized by the following figure:

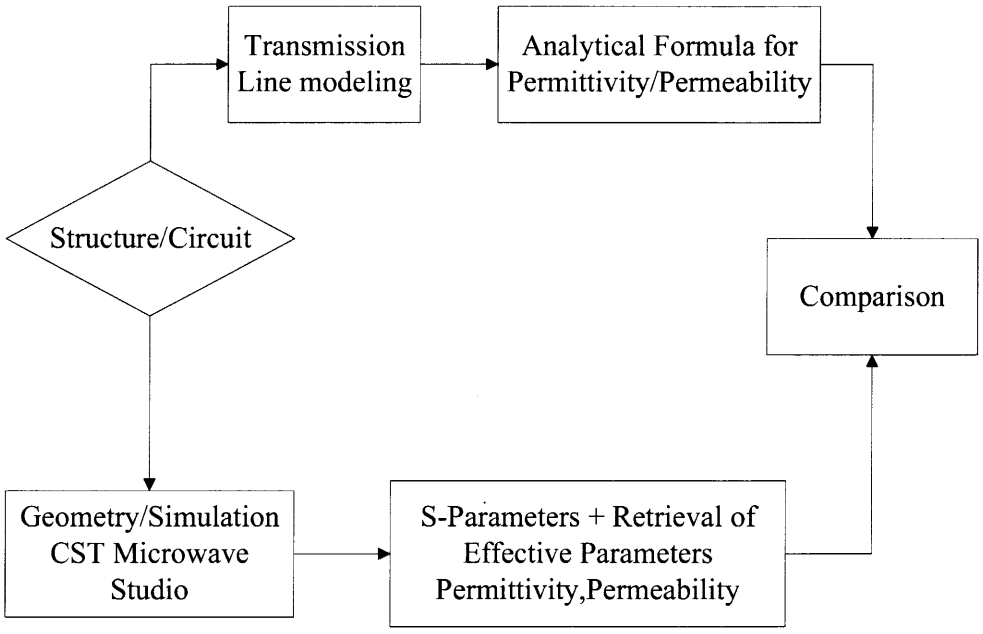

Figure 3.1.1 Block diagram of the proposed study.

First, we see how we can apply the upper branch for the analysis of a published structure.

Consider the resonator [23], which is a model of a LHM structure composed of SRRs and rod, in which the series element represents the SRR, and the shunt element represents the rod.

Figure 3.1.2-a Geometry of the resonator model 1 composed of split ring resonators and rod.

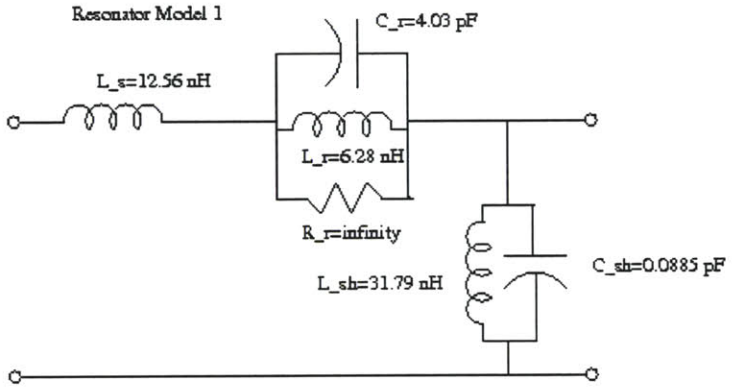

Figure 3.1.2-b Unit cell of the equivalent transmission line circuit of resonator model 1 composed of SRR/wire.

In analogy to the general case of T-loaded transmission line, we find the dispersion relation for the unloaded line of the resonator model 1 as plotted below in figure 3.1.3 with Z1 representing the SRR, Z2 the rod and Z3=0 by analogy with the T network loaded transmission line.

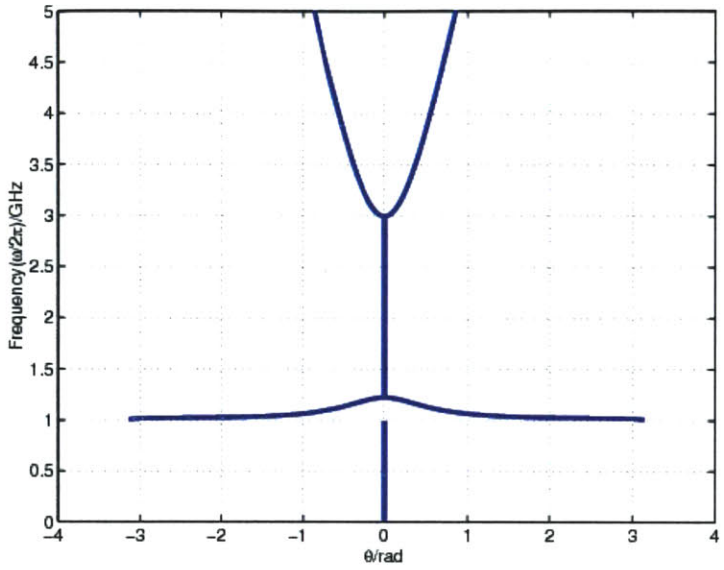

Figure 3.1.3 Dispersion curve for the resonator model 1.

From 0-1 GHz, the wave is evanescent on the line. From 1-1.22 GHz, the wave propagates on the line with group and phase velocity in opposite direction (negative refraction). The wave experiences another cut off from 1.22 GHz to 3 GHz, and finally from 3 GHz-5 GHz the wave propagates again on the line with both group and phase velocity in the same direction (positive refraction).

3.1.1 S Parameters and Impedance:

Using our transmission line modeling of resonators, we quickly can derive the S-parameters from the ABCD matrix, since a transmission line is nothing but a two port network by using equation (2.4.12).

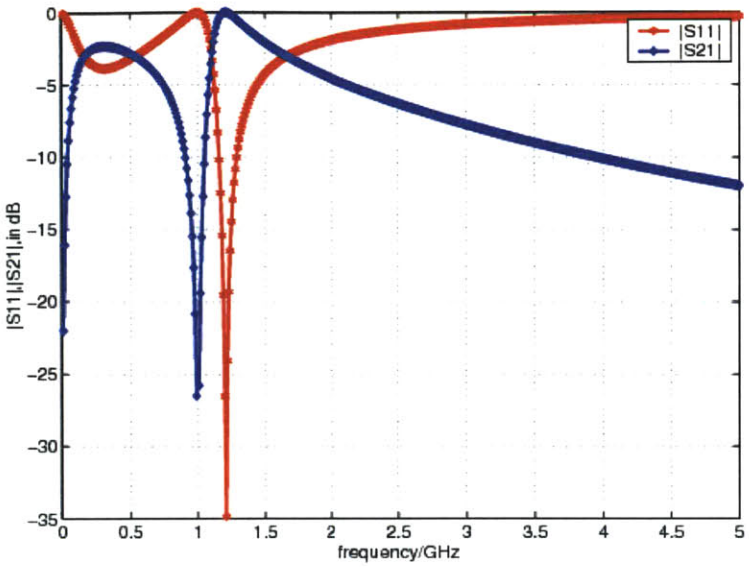

Figure 3.1.4 Magnitude of S-parameters for the resonator model1.

Notice the stopband at 1 GHz due to $\mu<0$ equivalently real part of the inductance per unit length L' being negative.

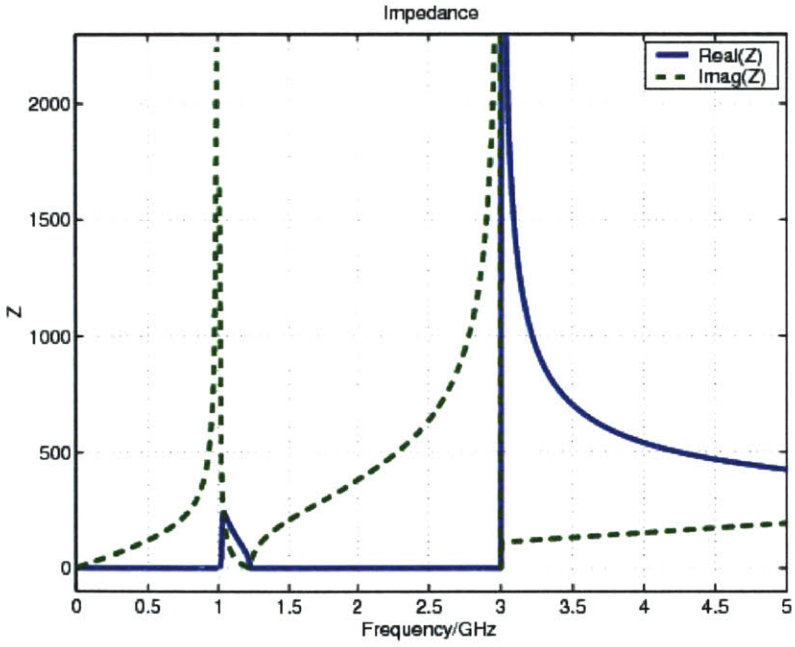

Figure 3.1.5 Real and Imaginary part of impedance (Z_n) for the resonator model 1.

From 0-1 GHz, the wave experiences cut-off because the real part of the impedance Z is zero. From 1-1.22 GHz, we observe propagation with low impedance. The wave undergoes another cut-off between 1.22-3 GHz identified as the plasma frequency, for the real part of epsilon equivalently Capacitance per unit length (C ') goes to zero. Finally from 3-5 GHz the wave propagates again with higher real part impedance values.

3.1.2 Retrieval of Index of Refraction:

The Index of refraction can be computed using the following formula:

$$n = \frac{\theta}{\omega d} c \quad (3.1.1) \text{ with the constraint that } imag(n) \geq 0 \quad (3.1.2)$$

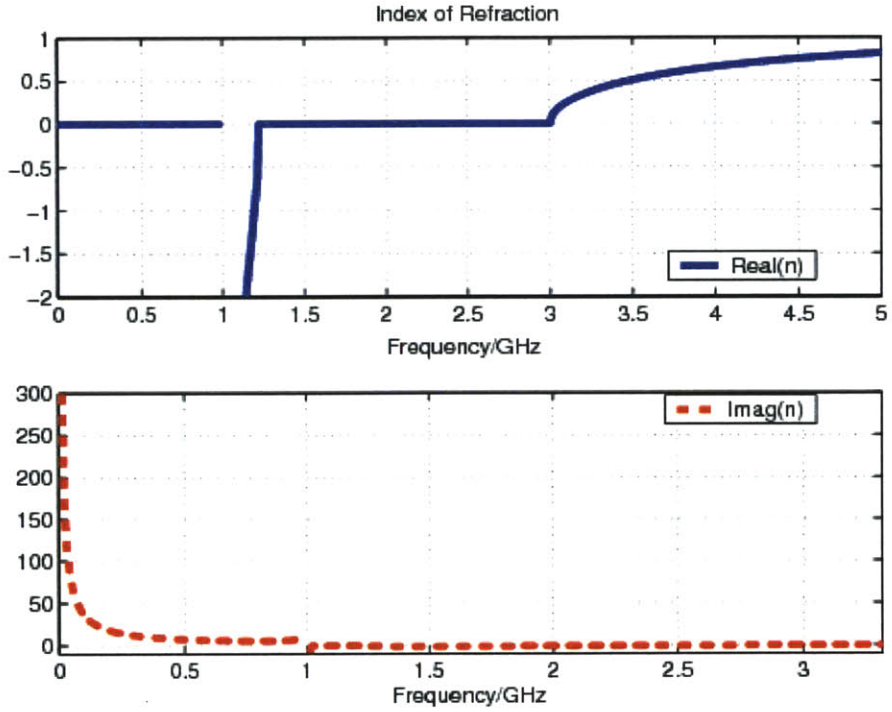

Figure 3.1.6 Retrieval of index of refraction (real and imaginary part) for the resonator model 1.

From the Impedance Z_n we derive the per unit length capacitance and Inductance using the fact that the wave impedance $\eta = \frac{k}{\omega \varepsilon_0} = \frac{\omega \mu_0}{k}$ (3.1.3)

$$L' = \frac{kZ_n}{\omega} \qquad (3.1.4) \text{ which corresponds to } \mu_{eff}$$

$$C' = \frac{k}{\omega Z_n} \qquad (3.1.5) \text{ which corresponds to } \varepsilon_{eff}$$

and $\eta = \sqrt{\frac{\mu_0}{\varepsilon_0}}$ is the free space intrinsic impedance.

3.1.3 Inductance and Capacitance per Unit Length

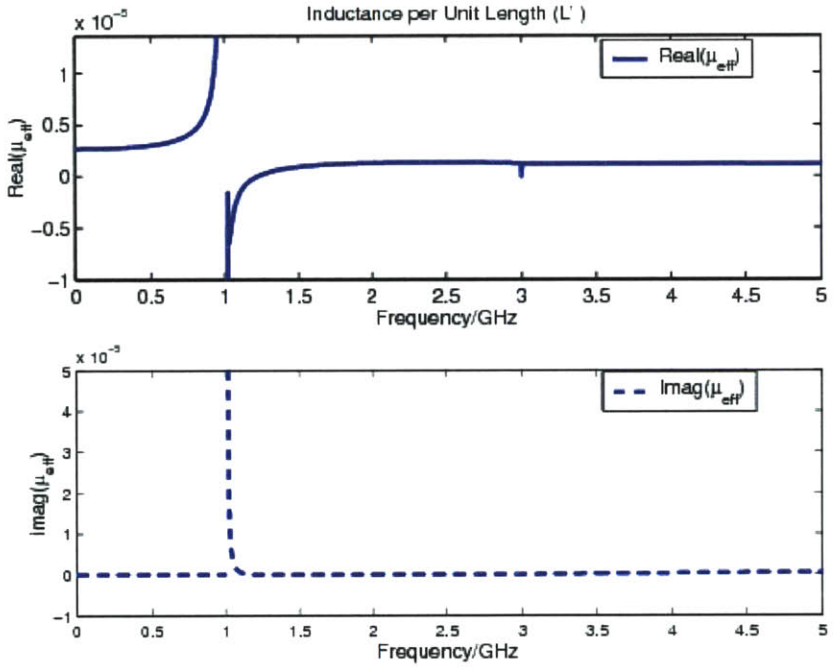

Figure 3.1.7 The inductance per unit length for the resonator model 1.

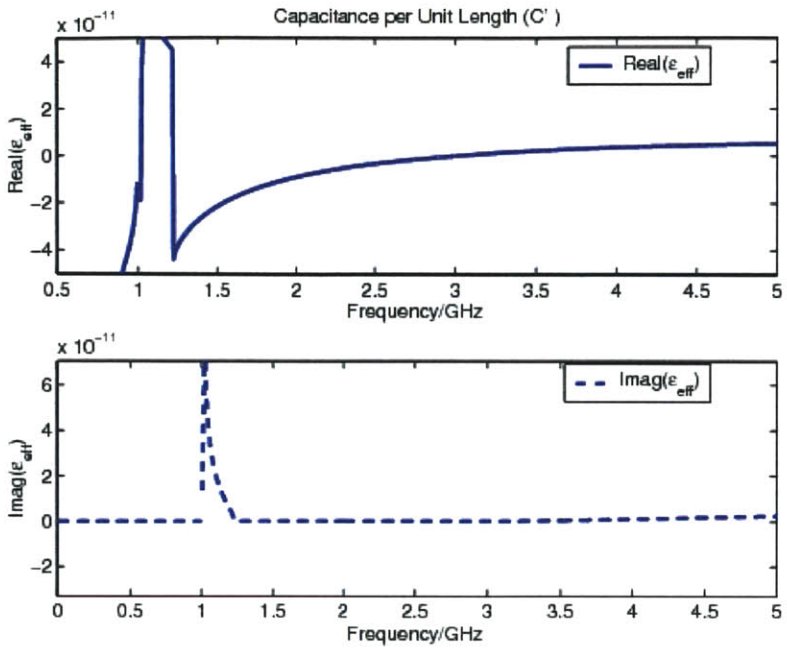

Figure 3.1.8 The Capacitance per unit length for the resonator model 1.

At 1 GHz, real(μ)<0 while real(ε)>0, as a result the wave experiences cut-off. Between 1-1.22 GHz, both real(μ) and real(ε) are negative, which corresponds to the left-handed band. As a result, the real part of the index of refraction is also negative. In this particular frequency band, phase and group velocity are opposite. This phenomenon is also called negative refraction.

3.2 Numerical Simulations of Rings Structures

One of the main concerns in the study of resonators is the quality factor Q and the effects of losses. In the study of metamaterials, it is well known that having a better LHM implies having a better resonator because low losses imply high Q.

As a result, the question remains about the choice of the structure that models the resonator. Is it a single ring or a double one? What are the choices of the type of split rings that need to be used? Is it the S-ring, the symmetric ring, or the omega ring?

One of the main argument for fabricating left handed materials, was to have a negative mu (μ) in a certain frequency band in such a way that it would overlap with the negative (ε) of the array of cut wires. In what follows, we will show that one ring is quite enough to achieve negative permeability behavior.

3.2.1 S-Structure

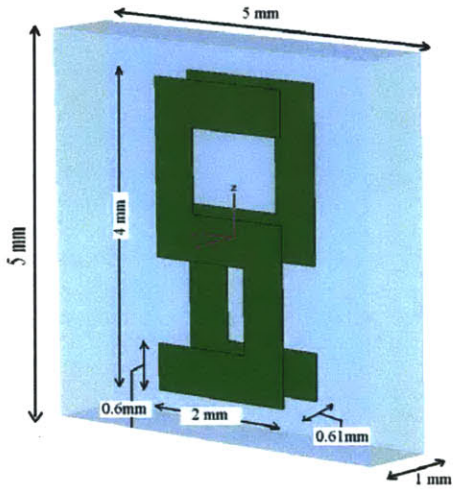

Figure 3.2.1 Unit cell of a periodic S-ring resonator. The structure is periodic in both the z and y-axis. The period in z is 5.5mm and 1.22mm in the y direction.

As predicted in references [2] and [18], that in addition to the negative permeability response, the S-SRR also exhibits a negative permittivity response that is in the same frequency band. As a result, the S-split ring resonator acts in a same way as the array of cut wires that display a negative epsilon below its plasma frequency.

Analytic calculations suggest that both ε_{eff} and μ_{eff} [32], [33] can be written as:

$$\varepsilon_{eff} = 1 - \frac{\omega_{ep}^2 - \omega_{eo}^2}{\omega^2 - \omega_{eo}^2 + i\gamma_e\omega} \quad (3.2.1)$$

$$\mu_{eff} = 1 - \frac{\omega_{mp}^2 - \omega_{mo}^2}{\omega^2 - \omega_{mo}^2 + i\gamma_m\omega} \quad (3.2.2)$$

where $\omega = 2\pi f$, $\omega_{eo}\left(\omega_{mo}\right)$ is the electric resonant low-frequency edge respectively (magnetic resonant frequency), and $\omega_{ep}\left(\omega_{mp}\right)$ represents the electric (respectively magnetic) plasma frequencies, and γ_e (γ_m) is the corresponding damping factor.

Using CST Microwave Studio, a commercial software that perform a full wave simulation based on finite difference time domain analysis, we run the simulation of the structure shown in figure 3.2.1 and obtain the scattering parameters. We did use the PEC boundary conditions on the xy plane and PMC boundary conditions on the xz plane. The wave vector is propagating on the x direction.

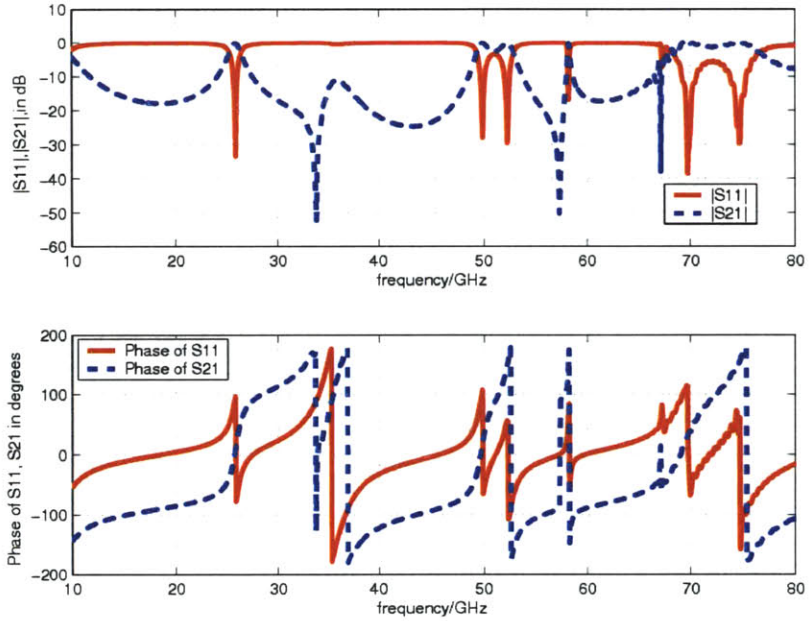

Figure 3.2.2 Simulation results of scattering parameters (magnitude and phase) for the S-structure shown in figure 3.2.1, with stopbands at 33.8, 57.3, and 67.1 GHz. An important remark is the passband displayed at 27.3 GHz in the S-structure transmission spectra.

3.2.2 Two Split Ring Resonators of Square Shape

Consider the broadside coupled of figure 3.2.3. As mentioned in reference [12], in order to avoid bianisotropic effects, the geometry has been chosen in such a way that the two split rings couple symmetrically.

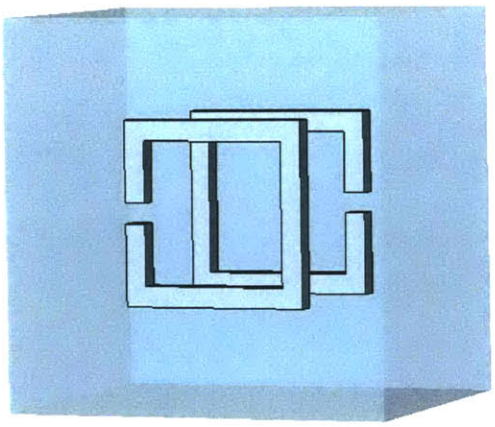

Figure 3.2.3 Broadside coupled double ring resonator of square shape.

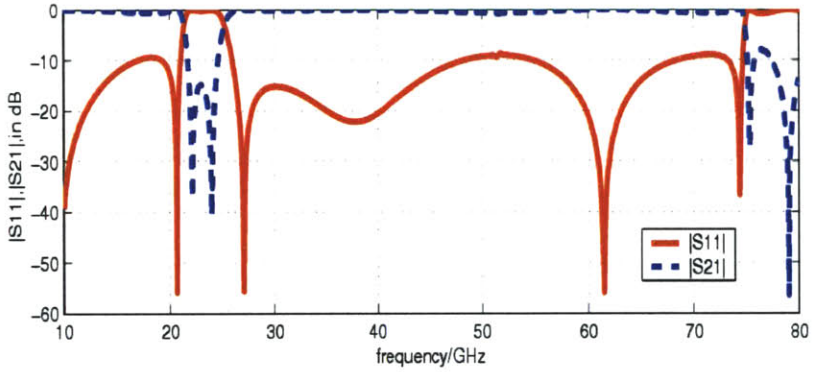

Figure 3.2.4 Simulation results of S-parameters (magnitude and phase) for the structure shown in figure 3.3.1 with, stopbands at 22.18, 24, 75.31 and at 79.02 GHz.

3.2.3 Double Circular Ring Resonator

The purpose of showing the double rings is to contrast it with the single ring thereby showing that you can still obtain a stopband.

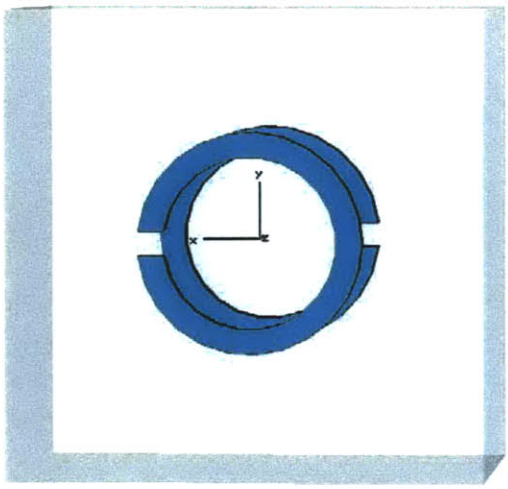

Figure 3.2.5 Broadside coupled of a double circular split ring resonator.

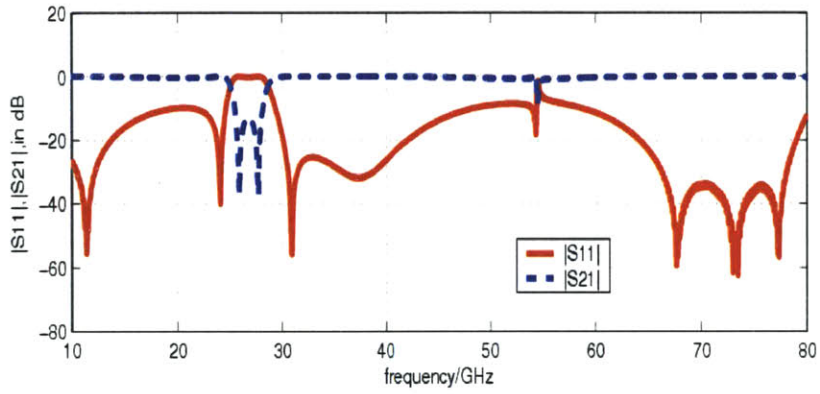

Figure 3.2.6 S-parameters from MWS simulation for the structure shown in Figure 3.2.5 with two stopbands at 25.89 and 27.71 GHz.

After analyzing the two different structures, the square symmetric ring, and the circular rings, we notice one thing in common in their respective transmission spectra, that is, they all display stopbands. Therefore in modeling resonators as lumped elements L-C equivalent circuit transmission lines, it is necessary to have a loop for the inductance and a gap or interruption to model the capacitance.

Chapter 4

Design of Single Ring Resonator

Since the development of metamaterials has been reported in the scientific literature, split ring resonators have played a tremendous role in obtaining negative permeability. Because such materials were not found in nature, there was an urgent need to fabricate them in order to verify their unique properties, since left handed materials require a simultaneous permittivity and permeability in the same frequency band. After Pendry [2] propose the circular split ring resonators(SRRs) for achieving negative permeability, Smith et al [3-4] have experimentally proposed and verified the first LHM structure operating in the microwave region. Since then, SRRs have constituted building blocks for fabricating metamaterials.

4.1 Analysis and Retrieval

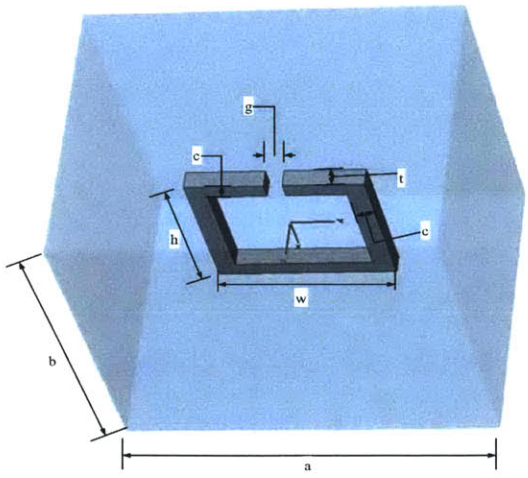

Figure 4.1.1 A 3D view of the proposed structure.

4.1.1 Analysis

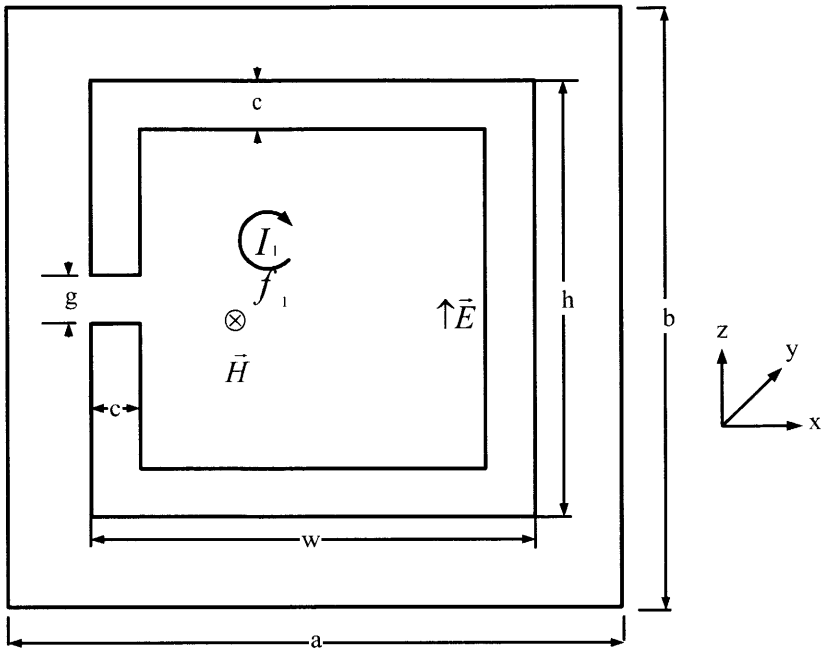

Figure 4.1.2 Planar circuit version of the proposed structure.

Assuming that the structure is infinitely long in the y direction and neglecting the fringing effects $\frac{\partial}{\partial y} = 0$, we can write the fields quantities as:

$$\vec{E} = \hat{z}E_z \qquad (4.1.1)$$
$$\vec{H} = \hat{y}H_y$$

Partitioning the volume into two different sets [18] and letting f_1 respectively f_0 be the fractional volume occupied by the planar structure respectively occupied by the remaining of the unit cell, and assuming a planar geometry of negligible thickness, we can write Maxwell equations:

$$\nabla \times \vec{E} = i\omega\mu_0\vec{H} \quad (4.1.2)$$
$$\nabla \times \vec{H} = -i\omega\varepsilon\vec{H} \quad (4.1.3)$$
$$\nabla \bullet \vec{B} = 0 \qquad (4.1.4)$$
$$\nabla \bullet \vec{D} = 0 \qquad (4.1.5)$$

From equation (4.1.2) we can calculate the flux as:

$$\int \nabla \times \vec{E} \bullet ds = \int \vec{E} \bullet d\vec{l} = \iint i\omega\mu \vec{H} \bullet ds = i\omega\mu Hab \quad (4.1.6)$$

Assuming a uniform H in each cell, we can write:

$$H_1 f_1 + H_0 f_0 = H \quad (4.1.7)$$

Applying the boundary conditions:

$$\int \left(\nabla \times \vec{H}\right) ds = \oint \vec{H}.d\vec{l} \Rightarrow H_1 - H_0 = j_1 \quad (4.1.8)$$

$$H_0 = H - j_1 f_1 \quad (4.1.9)$$

where $j_1 = \frac{I_1}{l}$ (4.1.10) is the surface current density.

Evaluating the emf of loop f_1 and using equation (4.1.7) we obtain:

$$\begin{aligned} \oint \vec{E} \bullet d\vec{l} &= i\omega\mu f_1 H_1 A \ with \ A = ab \\ &= r_s I_1 + \frac{1}{C_s} \int I_1 dt \qquad (4.1.11) \\ &= r_s I_1 + \frac{I_1}{C_s}\left(\frac{1}{-i\omega}\right) \end{aligned}$$

Combining (4.1.10) and (4.1.11) we can calculate the surface current density as:

$$j_1 = \frac{i\omega\mu H_1 f_1 A}{l(r_s + \frac{i}{C_s\omega})} \quad (4.1.12)$$

$$\mu = \mu_0 \ and \ \mu_{eff} = \frac{B_{ave}}{\mu_0 H_0} = \frac{H}{H_0}$$

$$\Rightarrow \ \mu_{eff} = 1 - \frac{-j_1 f_1}{H - j_1 f_1} \quad (4.1.13)$$

$$H = H_1 + j_1(f_1 - 1)$$

$$\text{But} \Rightarrow \mu_{eff} = 1 + \frac{j_1 f_1}{H_1 - j_1} \qquad (4.1.14)$$

$$= 1 - \frac{\dfrac{i\omega\mu_0 H_1 f_1^2 A}{l(r_s + \dfrac{i}{C_s\omega})}}{\dfrac{i\omega\mu_0 H_1 f_1 A}{l(r_s + \dfrac{i}{C_s\omega})} - H_1}$$

$$\Rightarrow \mu_{eff} = 1 - \frac{\omega^2 \mu_0 C_s f_1^2 A}{\left(\omega^2 \mu_0 C_s f_1 A - l\right) + i l r_s C_s \omega} \qquad (4.1.15)$$

under the form $\mu_{eff} = 1 - \dfrac{F\omega^2}{\left(\omega^2 - \omega_0^2\right) + i\omega\gamma}$ (4.1.16) as proposed in [2]

Therefore we can derive the induced elements from the above equations as follow:

$$\mu_{eff} = 1 - \frac{\omega^2 f_1}{(\omega^2 - \dfrac{l}{\mu_0 f_1 A C_s}) + \dfrac{i\omega l r_s}{\mu_0 f_1 A}}$$

$$with\ \omega_0^2 = \frac{l}{\mu_0 C_s f_1 A}$$

$$\gamma = \frac{l r_s}{\mu_0 f_1 A} \qquad (4.1.17)$$

$$L = \frac{\mu_0 f_1 A}{l}$$

$$C_s = \frac{\varepsilon_0 c t}{g}$$

From equation (4.1.17), we can tune the resonant frequency to a desired value by changing the parameters of the geometry (l, g, c, A).

4.2 Simulations and Retrieval

4.2.1 Single Split Ring Resonator of Square Shape

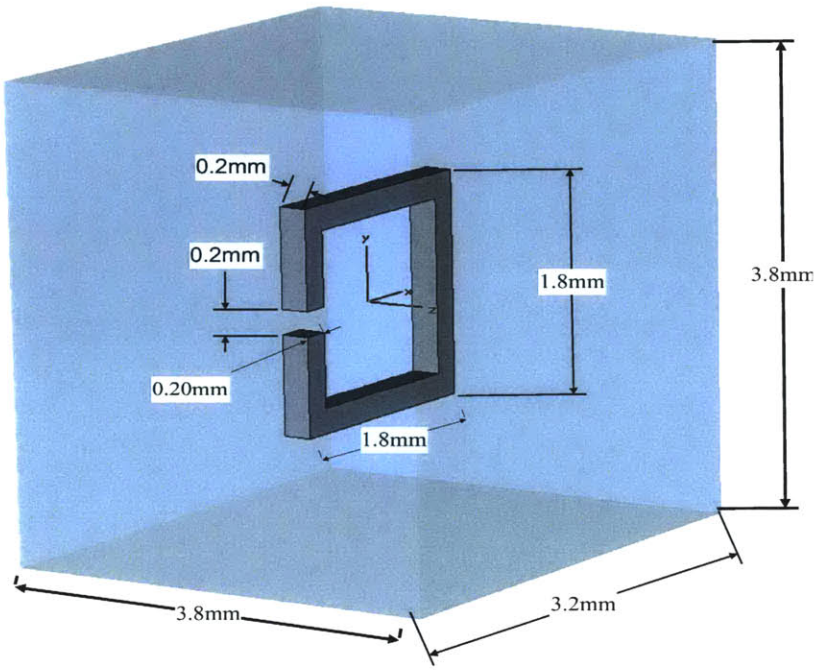

Figure 4.2.1 Single split ring resonator of square shape. The magnetic field is along the z-axis and the electric field is on the xy plane, and the k vector (propagation) is along the –x direction. For strong coupling, we put the E field along the y-axis and the H field is along the z-axis.

Consider the front view of the structure shown in figure 4.2.1. Using CST MWS with appropriate boundary conditions PMC in xy planes and PEC in xz planes we obtain the simulation results below:

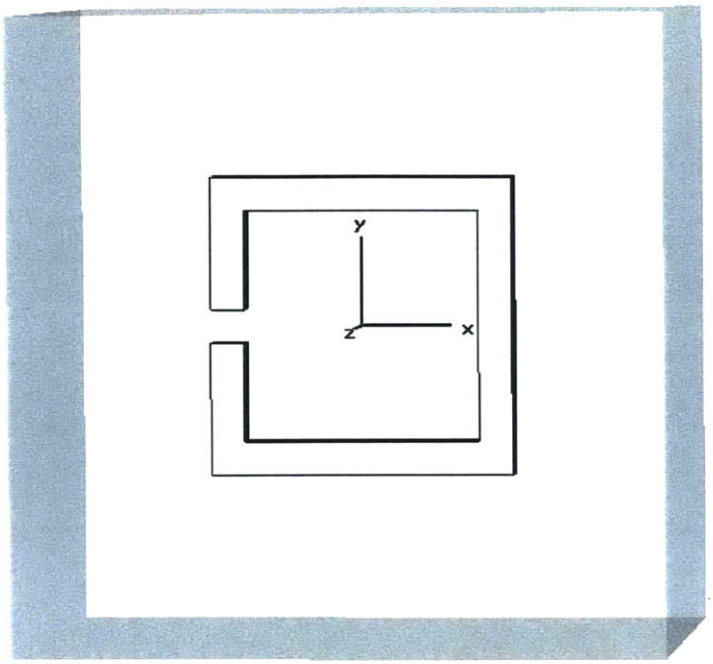

Figure 4.2.2 Front view of the structure shown above.

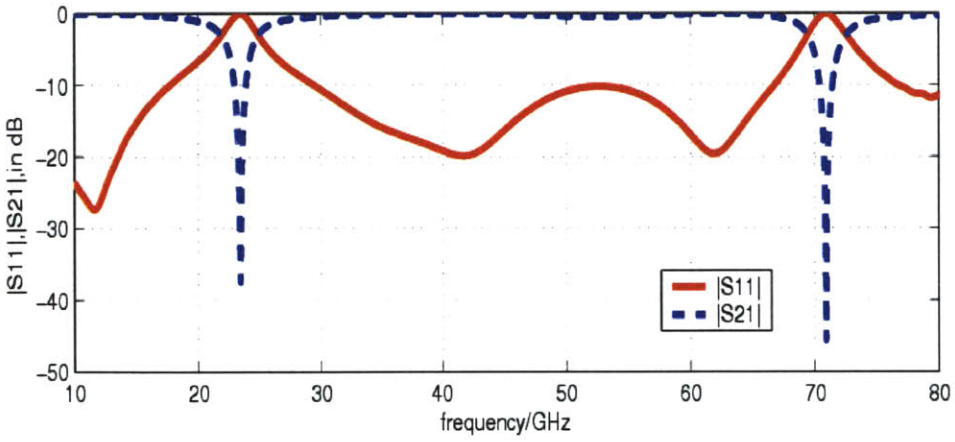

Figure 4.2.3 S-parameters (magnitude) from MWS simulation for the single square split ring with two stopbands at 23.4 and 70.9 GHz.

4.2.2 Single Circular Split Ring Resonator

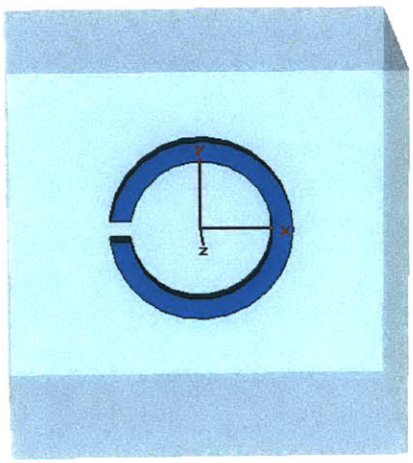

Figure 4.2.4 Single split circular ring with same dimensions as the square one.

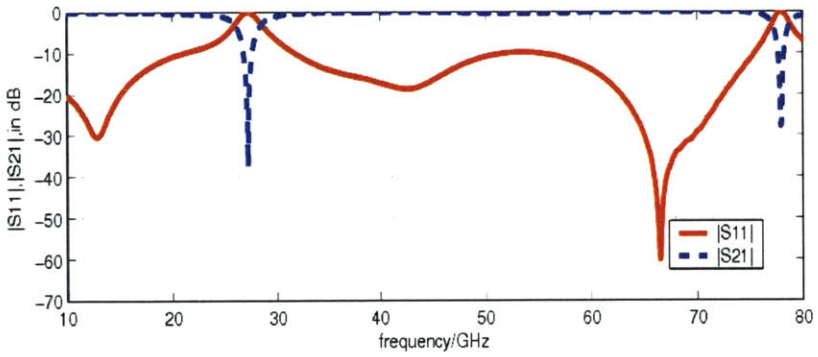

Figure 4.2.5 S-parameters (magnitude) from MWS simulation for the single circular SRR.

Even with the use of a single split ring whether square or circular, we still obtain two stop bands at 27.2 and at 77.9 GHz. Therefore the question remains that with both double ring and single ring we obtain stopbands. Consequently we decide not to use two rings in order to obtain a stop band with a negative effective permeability.

4.2.3 Close Ring Resonator

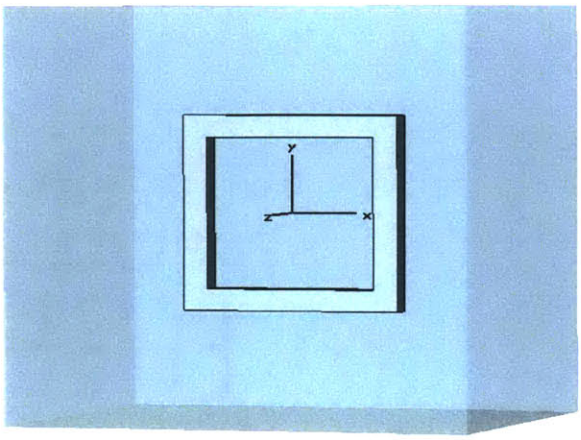

Figure 4.2.6 Close ring resonator (CRR).

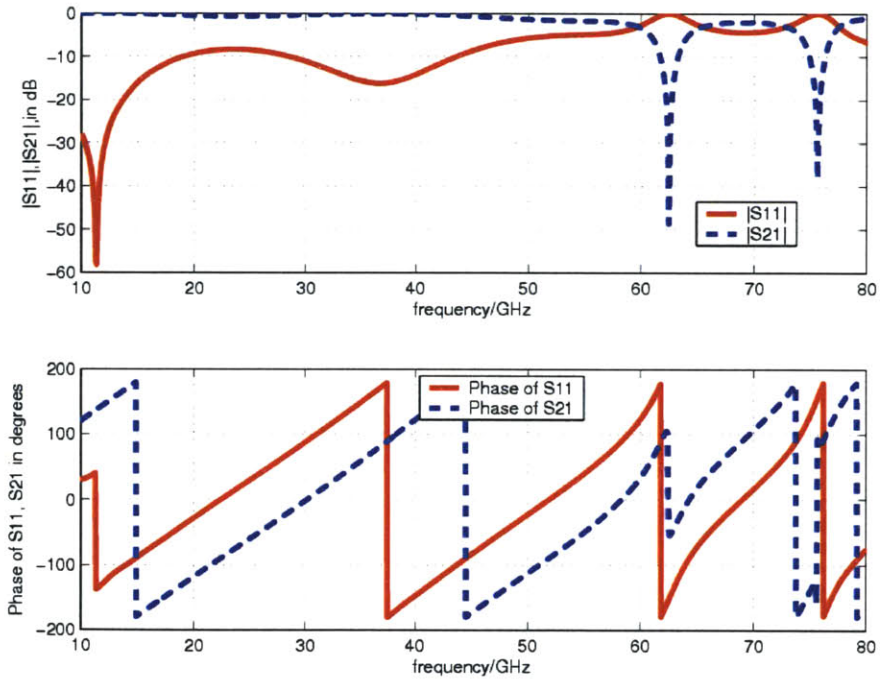

Figure 4.2.7 S-parameters from simulation of the structure shown in Figure 4.2.6.

We notice that the stopband at 23.4 GHz is no longer there compared to figure 4.2.3.

4.2.4 Discussions of Results

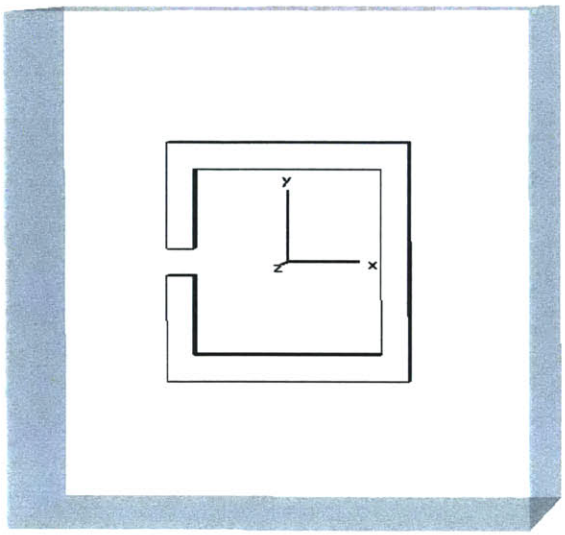

Figure 4.2.8 Split ring resonator (SRR).

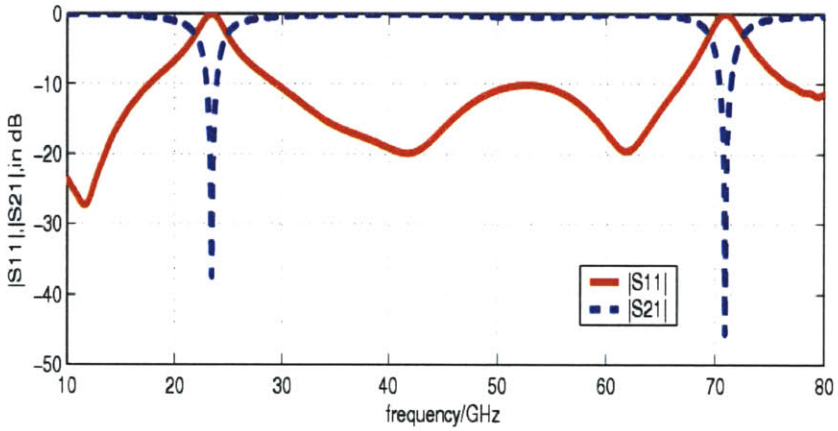

Figure 4.2.9 S-parameters simulation from CST Microwave Studio (MWS) for the single ring with split.

By comparing the plots corresponding to the close ring with the one corresponding to the split ring, it is equivalent to say that closing the gap in the ring removes the transmission dip. However, not all transmission dip are due to a negative (μ) as noticed in the above two plots that the second band gap is present in both the close ring as well as the SRR. This indicates clearly that the first band gap is due to μ negative, since closing the gap destroy the resonance effect and introduce cut-off because of μ negative.

From section 4.1.1 we derived the induced elements L, and C of the same structure using a transmission line approach. In comparison to Figure 2.4.23 we can say that the split ring resonator of our model has an equivalent circuit similar to that of figure 2.4.21. In order to elucidate this point further we will look at the retrieval of their respective effective parameters. On the one hand, the structure in figure 2.4.21 displays a stopband in its transmission spectra at 23.4 GHz and the retrieval of the unit length parameters show a negative inductance per unit length which is equivalent to μ_{eff} <0 in the vicinity of the resonant frequency 23.4 GHz, while its capacitance per unit length (ε_{eff}) is >0 in the same frequency range. Hence the cause of the stopband.

On the other hand, our proposed split ring resonator shown in figure 4.2.1 also displays the same characteristics in its transmission spectra. From the S-parameters simulation results (figure 4.1.3) we also notice a stopband in its transmission spectra at the same resonant frequency. Using an inversion method, we retrieved the effective parameters of the structure of figure 4.2.1, and comparing the results with those of figures 3.1.7 and 3.1.8, we conclude that our proposed structure can be modeled as a transmission line loaded by a resonant series connection of an inductance (area of the loop of the ring) and capacitance (gap or split in the ring).

4.2.5 Retrieval

We perform a robust retrieval [16] of the effective parameters for the structure shown in figure 4.1.3. At the stop band of 23.4 GHz, we can calculate the induced elements C, and L by:

$$C = \frac{\varepsilon_0 tc}{g}; \quad L = \frac{1}{4\pi^2 f_0^2 C}; \quad (4.1.18)$$

$$\text{With } t = c = g = 0.2mm; \; f_0 = 23.4GHz$$

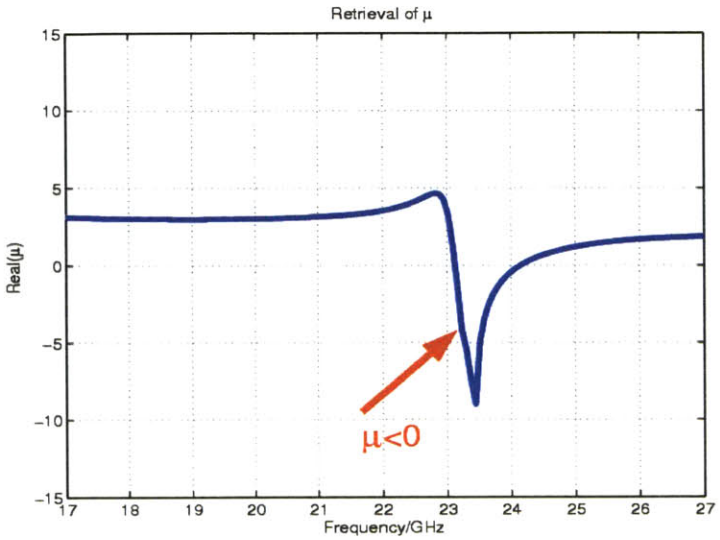

Figure 4.2.10 Retrieval of effective parameters. Real part of permeability.

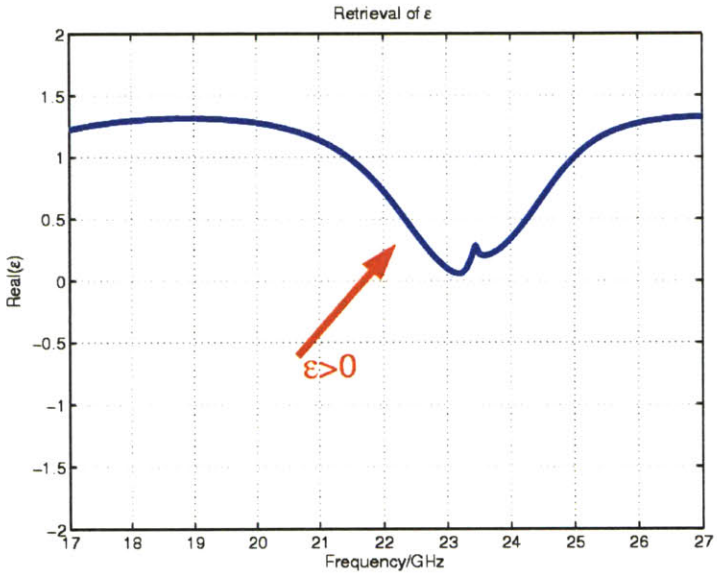

Figure 4.2.11 Retrieval of effective parameters. Real part of permittivity.

We notice the magnetic resonance and electric anti-resonance at 23.4 GHz where $\mu<0$ and $\varepsilon>0$, hence a stopband. Therefore, the stopband is due to μ negative.

Chapter 5

Conclusion

Using transmission line approach we were able to derive the capacitance and inductance per unit length, and also the line impedance. With a thorough analysis of transmission lines, we were also able to model a real structure by analyzing its S- parameters obtained from simulation (Microwave Studio), and compare them to those derived from our transmission line equivalent circuit building blocks. Often times, resonators are modeled by a combination of L-C circuits which is tedious to figure out what is the exact model, whether a L-C series, parallel, a combination of the two, or a hybrid structure. Experience has shown that it can be very tedious to get the correct model. Using a transmission line approach has helped a great deal to find the accurate model by simply comparing the S-parameters of the lump element circuit to that of the simulation of the real structure. Since the electrical size is small in the sense that distances between loads were very small compared to the wavelength of the electromagnetic wave, we were able to use the effective medium model. In comparing real and imaginary parts of effective medium quantities (permeability and permittivity), we found that the resonant behavior of the effective magnetic permeability is coupled with an antiresonant behavior of the effective permittivity and vice versa. In sum, we obtain the same results whether using the retrieval method from the simulation of the real structure or using the equivalent transmission line circuit by studying the dispersion and thereby get the per unit length parameters of the effective line. This process could be generalized and applied to any waveguide structures or strip-lines that support TEM waves.

Bibliography

[1] V. G. Veselego, *Sov. Phys. Usp.*, vol. 10, no. 4, pp.509-514, Jan.-Feb. 1968.

[2] J. B. Pendry, A. J. Holden, D. J. Robins, and W. J. Stewart, *IEEE Trans. Microwave Theory Tech.*, vol. 47, pp. 2075-2084, Nov. 1999.

[3] D. R. Smith, W. J. Padilla, D. C. Vier, S. C. Nemat-Nasser, and S. Schultz, *Phys. Rev. Lett.*, vol. 84, no. 18, pp. 4184-4187, May 2000.

[4] D. R. Smith and N. Kroll, *Phys. Rev. Lett.*, vol. 85, no. 14, pp. 2933-2936, Oct. 2000.

[5] R. A. Shelby, D.R. Smith, S.C. Nemat-Nasser, and S. Schultz, *Appl. Phys. Lett.*, vol. 78, no. 4, pp. 489-491, Jan. 2001.

[6] R. A. Shelby, D. R. Smith, and S. Schultz, *Science*, vol. 292, no. 4, pp. 77-79, Apr. 2001.

[7] J. B. Pendry, *Phys. Rev. Lett.* 85, 3966–3969 (2000).

[8] S. A. Ramakrishna, and J. B. Pendry, *Phys. Rev.* B. vol. 67, 201101 (R) (2003).

[9] J. B. Pendry and S. A. Ramakrishna *Journal of Physics: Condensed Matter*, Vol. 14 (2002) 8463-8479.

[10] N. Katsarakis, T. Koschny, and M. Kafesaki, E. N. Economou, C. M. Soukoulis, *Appl. Phys. Lett.* Vol. 84, no. 15 (2004).

[11] R. Marques, F. Mesa, J. Martel, and F. Medina, *IEEE Trans. Antennas Propag.* Vol. 51, no.10, pp.2572-2581, Oct.2003.

[12] J. D. Baena, R. Marques, F. Medina, and J. Martel *Phys. Rev.* B 69 014402.

[13] N. Katsarakis, T. Koschny, M. Kafesaki, E.N. Economou, E. Ozbay, and C. M. Soukoulis, *Phys. Rev. Lett* B 70 201101(R) (2004).

[14] K. Aydin, I. Bulu, K. Guven, M. Kafesaki, C.M. Soukoulis, and E. Ozbay, *New Journal of Physics.,* vol.7 (2005).

[15] T. Koschny, M. Kafesaki, E.N. Economou, and C.M. Soukoulis, *Phys. Rev. Lett.*, vol. 93, no. 10 (2004).

[16] X. Chen, B.I. Wu, J. A. Kong, and T. M. Grzegorczyk, *Phys. Rev.* E 71, 046610 (2005).

[17] M. Kafesaki, T. Koschny, R.S. Penciu, T.F. Gundogdu, E.N. Economou, and C.M. Soukoulis, *J. Opt. Pure Appl. Opt* 7 (2005).

[18] H. S. Chen, L. X. Ran, T. T. Huangfu, X. M. Zhang, K. S. Chen, J. A. Kong, and T. M. Grzegorczyk, PIER 51, 231-247, 2005.

[19] J. A. Kong, *Electromagnetic Wave Theory* (EMW, Cambridge, MA, 2000).

[20] D. R. Smith, D. C. Vier, N. Kroll, and S. Schultz, *App. Phys. Lett.*, vol. 77, no. 14 Oct. 2000.

[21] D. R. Smith and S. Schultz, P. Markos and C.M. Soukoulis, *Phys. Rev.* B, vol. 65 195104.

[22] X. Chen, T. M. Grzegorczyk, B.I. Wu, J. Pacheco, and J. A. Kong, *Phys. Rev* E 70, 016608 (2004).

[23] G. V. Eleftheriades, O. Siddiqui, and A. K. Iyer, *IEEE Microwave and Wireless Components Letters*, vol. 13, no. 2, Feb. 2003.

[24] G. V. Eleftheriades, Ashwin K. Iyer, and Peter C. Kremer, *IEEE Trans. on Microwave Theory and Tech.*, Vol. 50, No. 12, pp. 2702-2712, Dec. 2002.

[25] Iyer, A.K. Eleftheriades, G.V. *Microwave Symposium Digest, 2002 IEEE MTT-S International*, Seattle, WA, USA, vol.2, 2-7 June 2002, pp 1067 – 1070.

[26] H. O. Moser, B. D. F. Casse, O. Wilhelmi, and B. T. Saw, Phys. Rev. Lett.94, 063901 (2005).

[27] T. J. Yen, W. J. Padilla, N. Fang, D. C. Vier, D. R. Smith, J. B. Pendry, D. N. Basov, X. Zhang, *Science*, v.303, 1494 (2004).

[28] Philippe Gay-Balmaz and Olivier J. F. Martin *Journal of Applied Physics*, Vol. 92, issue 5, pp. 2929-36 (2002).

[29] S. J. Orfanidis, *Electromagnetic Waves & Antennas*, June 21, 2004 (Online version-www.ece.rutgers.edu/~orfanidi/ewa).

[30] S. Tretyakov, *Analytical Modeling in Applied Electromagnetics*, July 30, 2003 (Artech House Electromagnetic Analysis Series).

[31] J. W.Nilsson, *Electric Circuits*, 4th ed., 1993 (Addison-Wesley Series in Electrical and Computer Engineering).

[32] E. Di Gennaro, P. V. Parimi, W. T. Lu, and S. Sridhar, J. S. Derov and B. Turchinetz *Phys. Rev.* B 72, 033110 (2005).

[33] Pendry, J.B., A. J. Holden, W. J. Stewart, and I. Youngs, *Phys. Rev. Lett.*; Vol. 76, 4773-4776, 1996.

[34] D. M. Pozar, *Microwave Engineering,* 3rd ed., 2005(J. Wiley).

[35] R. E. Collin, *Foundations for Microwave Engineering,* 2nd ed., 2000 (Wiley-IEEE Press).